Sea Ice Classification From RADARSAT Constellation Mission Images Using Normalizer-Free ResNet

by

© **Hangyu Lyu, B.Eng., M.A.Sc.**

A thesis submitted to the School of
Graduate Studies in partial
fulfillment of the requirements for
the degree of Master of Engineering.

Faculty of Engineering and Applied Science

Memorial University

October 20, 2022

St. John's, Newfoundland and Labrador, Canada

Abstract

Sea ice monitoring plays a vital role in climate study, maritime navigation and offshore industries. Sea ice monitoring consists of different applications, such as ice classification, concentration and thickness retrieval. As one of the branches of sea ice monitoring, sea ice classification is an essential task in sea ice mapping and the premise to obtain other sea ice parameters. Satellite images are the primary source for sea ice classification due to the broad coverage, the extremely harsh environment in the polar regions and the near real-time requirements of some applications. Spaceborne Synthetic Aperture Radar (SAR) has been widely used as an effective tool for sea ice sensing for decades because it can collect data day and night and in all weather conditions. As a typical representative of the next generation SAR mission, the RADARSAT Constellation Mission (RCM) provides three C-band SAR satellites with shorter revisit time and broader spatial coverage, which will be widely used in various earth observation applications including sea ice sensing. The Sentinel-1 mission comprises two C-band SAR satellites with dual-polarized imaging capability, providing open and free data from the European Space Agency (ESA). Both RCM and Sentinel-1 C-band SARs operate at a center frequency of 5.405 GHz. In addition, RCM provides more spatial coverage and a shorter revisit time than Sentinel-1. However, actual RCM data have not been used for sea ice classification, and no study for comparing the sea ice classification performances of RCM and Sentinel-1 has been conducted.

Deep convolutional neural networks (CNN) have been extensively employed in sea ice monitoring applications in the last decade. An example of deep CNN, Normalizer-Free ResNet (NFNet) was proposed by DeepMind in early 2021 and achieved a new state-of-the-art accuracy on the ImageNet dataset. In this thesis, a NFNet based approach has been proposed for sea ice classification using dual-polarized SAR data. In the first part of this study, the RCM data are utilized for sea ice detection and classification using NFNet for the first time. HH (horizontal transmit and horizontal receive), HV (horizontal transmit and vertical receive) and the cross-polarization ratio are extracted from the dual-polarized

RCM data with a medium resolution (50 m) for NFNet-F0 model. Experimental results from the eastern Arctic show that destriping in the HV channel is necessary to improve the quality of sea ice classification. A two-level random forest (RF) classification model is also applied as a conventional technique for comparisons with NFNet. The sea ice concentration, estimated based on the classification result from each region, was validated with the corresponding polygon of the Canadian weekly regional ice chart. The overall classification accuracy confirms the superior performance of the NFNet model over the RF model for sea ice monitoring and the sea ice sensing capacity of RCM. The second part of this study focuses on comparing sea ice classification results from the two C-band SAR missions (RCM and Sentinel-1) with the state-of-the-art convolutional neural network, NFNet. HH, HV and the cross-polarization ratio are extracted from the overlapping area of dual-polarized RCM and Sentinel-1 images acquired on similar dates. The sea ice classification results show that the RCM Medium Resolution 50m mode performs better than the Sentinel-1 EW GRD Medium Resolution 90m mode.

Acknowledgements

Two years of the master's program come to an end. During the process of study, I have encountered many difficulties, but I have also made progress after solving these difficulties. My progress is inseparable from the help and support of others.

First of all, I particularly express my sincere gratitude to my supervisor, Dr. Weimin Huang. His patience and guidance have enabled me to be strict with myself and standardize my writing and research methodology. Feedback from Dr. Huang accurately indicated my shortcomings and pushed my research further. I would like to thank my co-supervisor, Dr. Masoud Mahdianpari, who provided many valuable suggestions. His suggestions helped me solve the difficulties of using SAR data and deepened my understanding of machine learning. I also want to thank the Faculty of Engineering and Applied Science for providing me with the opportunity to take courses and research.

This research was undertaken thanks in part to funding from the Canada First Research Excellence Fund, through the Ocean Frontier Institute. This work was also supported by the Natural Sciences and Engineering Research Council of Canada (NSERC) under Grants [NSERC RGPIN-2017-04508] and [NSERC RGPAS-2017-507962] to W. Huang. Moreover, I would like to thank the Canadian Space Agency (CSA) and the Canadian Ice Service for providing RCM data and sea ice charts. In addition, I would like to thank Compute Canada for the provision of high-quality GPU resources.

Next, I would like to thank all the members of our remote sensing research group. Their presentations and suggestions inspired me and improved my study. Finally, I would like to express deep gratitude to my family. Without their support and understanding, I couldn't have completed the research.

Table of contents

Title page **i**

Abstract **ii**

Acknowledgements **iv**

Table of contents **v**

List of tables **viii**

List of figures **ix**

List of symbols **xii**

List of abbreviations **xiii**

1 Introduction **1**

1.1 Research Rationale 1

1.2 Sea Ice Classification Background 5

1.3 Motivation and Objectives 8

1.4 The Scope of the Thesis 11

2 Eastern Arctic Sea Ice Sensing: First Results From the RADARSAT Constellation Mission Data **13**

2.1 Study Area and Data Set 14

2.1.1 Study Area 14

2.1.2 Sea Ice Chart 14

2.1.3 RCM Data and Sea State Information 16

2.1.4 Training and Validation Datasets 18

2.2 Methodology 20

2.2.1 Preprocessing 20

2.2.2 Normalizer-Free ResNet 23

2.2.3 Random Forest 27

2.3 Experiment Result and Discussion 29

2.4 Classification Results in the Davis Strait, 2021 42

2.5 Chapter Summary 42

3 Comparison of Sea Ice Classification From RADARSAT Constellation Mission and Sentinel-1 SAR Imagery **56**

3.1 Data Description 57

3.1.1 Sea Ice Chart 57

3.1.2 RCM and Sentinel-1 Data 57

3.1.3 Training and Validation 59

3.2 Methodology 59

3.2.1 Preprocessing 59

3.2.2 Normalizer-Free ResNet 60

3.3 Experiment Result 65

3.4 Chapter Summary 69

Bibliography **70**

List of tables

2.1 Sea ice types and the corresponding stage of development (age) egg codes [1]. 16

2.2 Characteristics of RCM imagery used in this study. 16

2.3 The configuration of the NFNet-F0 layers. 24

2.4 Two-level RF classification parameters. 29

2.5 Comparison of the estimated concentration for March 1. 36

2.6 Comparison of the estimated concentration for March 2. 37

2.7 Comparison of the estimated concentration for 4 January. 38

3.1 RCM and Sentinel-1 images information. 57

3.2 Comparison of the estimated concentration results for IP4. 66

3.3 Comparison of the estimated concentration results for IP5. 66

3.4 Comparison of the estimated concentration results for IP6. 67

List of figures

2.1 (**a**) The March 1st and 2nd RCM images laid over sea ice charts. Light green represents ice, light blue represents water and pink represents land. The yellow star represents the location with sea-state information. The March 1st image was used for selecting training samples, and the first testing set samples of NI and water. The March 2nd image was used for selecting the first testing set samples of OI/FYI. Green dots indicate the locations for selecting the training samples. Red dots indicate the locations for choosing the testing samples. (**b**) Regional sea ice chart in the Eastern Arctic for the week of March 1st 2021. Red rectangles indicate the coverages of the March 1st and 2nd RCM images. (**c**) The January 4th RCM image laid over a sea ice chart (color codes are same as those in (**a**)). The stars are the locations with sea-state information near the testing samples. The January 4th image was used for selecting the second testing set samples. Red dots also indicate the locations where the testing samples were collected. (**d**) Regional sea ice chart in the Eastern Arctic for the week of January 4th 2021. The red rectangle illustrates the coverage of the January 4th RCM image. 17

2.2 RCM preprocessing steps. 21

2.3 Destriping examples. Image acquired on 2 March 2021. 22

2.4 Schematic diagram of the NFNet-F0 model (compressed view). 25

2.5 NFNet residual blocks (transition and non-transition). 25

2.6 Epochs versus validation accuracy. 28

2.7 (**a**) Image acquired on March 1 2021. The green rectangles display the locations of the training samples for OI/FYI. The red and white rectangles indicate the areas of the training and testing samples for NI and water, respectively. (**b**) Sea ice chart. (**c**) Land mask. (**d**) RF classification result. (**e**) NFNet classification result. 30

2.8 (**a**) Image acquired on March 2 2021. The green rectangles display the locations of the testing samples for OI/FYI. (**b**) Sea ice chart. (**c**) Land mask. (**d**) RF classification result. (**e**) NFNet classification result. 31

2.9 (**a**) Image acquired on January 4 2021. The green, red and white rectangles indicate the areas of the testing samples of OI/FYI, NI and water, respectively. The testing samples were at least 100 kilometers away from the March 1st training samples. (**b**) Sea ice chart. The area without sea ice chart data is indicated in gray. (**c**) Land mask. (**d**) RF classification result. (**e**) NFNet classification result. 32

2.10 Confusion matrices of the RF and NFNet models. 34

2.11 2-D feature visualizations of the sea ice classes from the two testing sets, using the t-SNE algorithm for the second last layer of the NFNet. (**a**) The t-SNE diagram of the first testing set. (**b**) The t-SNE diagram of the second testing set. 35

2.12 January 4 and January 24, 2021. 43

2.13 February 1 and February 21, 2021. 44

2.14 March 9 and March 29, 2021. 45

2.15 April 6 and April 22, 2021. 46

2.16 May 16 and May 24, 2021. 47

2.17 June 17 and June 29, 2021. 48

2.18 July 22 and August 3, 2021. 49

2.19 August 19 and September 4, 2021. 50

2.20 September 28 and October 14, 2021. 51

2.21 October 30 and November 11, 2021. 52

2.22 November 23 and December 1, 2021. 53

2.23 December 13 and December 25, 2021. 54

3.1 The locations of the fourth pair (IP4) of dual-polarized RCM and Sentinel-1 images laid over sea ice chart. 58

3.2 Flowchart of NFNet-based sea ice classification and results comparison. . . . 61

3.3 Confusion matrices of the NFNet models trained from RCM and Sentinel-1 datasets. 61

3.4 (a) Sentinel-1 image acquired on December 28, 2020. (b) RCM image acquired on the same date. The green, red and white rectangles indicate the areas of the testing samples of OI/FYI, NI and water, respectively. (c) Sea ice chart. (d) Land mask. (e) Sentinel-1 classification result. (f) RCM classification result. 62

3.5 (a) Sentinel-1 image acquired on January 18, 2021. (b) RCM image acquired on January 18, 2021. (c) Sea ice chart. (d) Land mask. (e) Sentinel-1 classification result. (f) RCM classification result. 63

3.6 (a) Sentinel-1 image acquired on February 15, 2021. (b) RCM image acquired on February 15, 2021. (c) Sea ice chart. (d) Land mask. (e) Sentinel-1 classification result. (f) RCM classification result. 64

List of symbols

σ^0	backscattering coefficient (p. 4)
σ^0_{hh}	backscattering coefficient at HH (p. 5)
σ^0_{vv}	backscattering coefficient at VV (p. 5)
σ^0_{RH}	backscattering coefficient at RH (p. 8)
σ^0_{RV}	backscattering coefficient at RV (p. 8)
R^2	coefficient of determination (p. 9)
A	range dependent gain value in the RCM metadata file for calibration (p. 21)
B	offset in the RCM metadata file for calibration (p. 21)
D	digital value for each pixel in the RCM metadata file for calibration (p. 21)
α, β	scalers in NFNet's transition and non-transition blocks (p. 23)
G^l_i	the ith row of the gradient of the l-th layer (p. 26)
W^l_i	the ith row of the weight of the l-th layer (p. 26)
λ	clipping threshold (p. 26)
t	number of iterations (p. 27)
m_{ij}	the pair (i, j) in a specific direction appears m times in the GLCM matrix (p. 28)

List of abbreviations

WMO	World Meteorological Organization (p. 2)
SAR	Synthetic Aperture Radar (p. 4)
HH	Horizontal Transmit and Horizontal Receive (p. 4)
HV	Horizontal Transmit and Vertical Receive (p. 4)
CSA	Canadian Space Agency (p. 5)
ESA	European Space Agency (p. 5)
GLCP	Gray-level Co-occurring Probabilities (p. 6)
IRGS	Iterative Region Growing using Semantics (p. 6)
MRF	Markov Random Field (p. 6)
VH	Vertical Transmit and Horizontal Receive (p. 6)
VV	Vertical Transmit and Vertical Receive (p. 6)
WGLCP	Weighted Gray-level Co-occurring Probabilities (p. 6)
RCM	RADARSAT Constellation Mission (p. 7)
HCP	Hybrid Compact Polarization (p. 7)
RH	Right Circular Transmit and Horizontal Receive (p. 7)
RV	Right Circular Transmit and Vertical Receive (p. 7)
CH	Circular Transmit and Horizontal Receive (p. 8)
CV	Circular Transmit and Vertical Receive (p. 8)
GRD	Ground Range Detected (p. 8)
GLCM	Gray-level Co-occurrence Matrix (p. 8)
SVM	Support Vector Machine (p. 9)

RF	Random Forest (p. 9)
DT	Decision Tree (p. 9)
CNN	Convolutional Neural Network (p. 10)
VGG-16	Visual Geometric Group–16 Layer (p. 10)
ResNet	Residual Neural Network (p. 10)
NFNet	Normalizer-Free ResNet (p. 10)
ADC	Adaptive Gradient Clipping (p. 11)
GIS	Geographic Information System (p. 11)
UTC	Universal Time Coordinated (p. 14)
CIS	Canadian Ice Service (p. 15)
NI	New Ice (p. 15)
FYI	First-year Ice (p. 15)
OI	Old Ice (p. 15)
GI	Grey Ice (p. 16)
GWI	Grey-white Ice (p. 16)
TFYI	Thin First-year Ice (p. 16)
MFYI	Medium First-year Ice (p. 16)
TKFYI	Thick First-year Ice (p. 16)
SNAP	Sentinel Application Platform (p. 20)
DEM	Digital Elevation Model (p. 22)
GELU	Gaussian Error Linear Unit (p. 23)
BN	Batch Normalization (p. 26)
LSTM	Long Short-Term Memory (p. 28)
t-SNE	t-Distributed Stochastic Neighbor Embedding (p. 34)
NESZ	Noise Equivalent Sigma Zero (p. 60)

Chapter 1

Introduction

1.1 Research Rationale

Sea ice is floating frozen seawater on the ocean surface, which plays a crucial role on both regional and global scales because of its influence on the polar environment, ocean circulation, marine ecosystem, and climate. On a global scale, sea ice is regarded as a natural indicator of climate change. Exchanges of heat, moisture, and salinity in oceans are regulated by sea ice [2]. Salt can be expelled due to the formation of ice crystals. The salt expelling can affect oceanic circulation and further affect the tropical environment [3]. Sea ice can form a cap layer of insulation on the surface of the ocean, which can not only limit the effect of coastal wind and waves but also reduce evaporation and heat loss to the atmosphere [4]. Moreover, the high albedo of sea ice reduces the absorption of solar energy. Polar sea ice reflects more than 80% of incident energy and affects solar power absorption [5]. In other words, global radiative flux balance is highly affected by sea ice extent. Once global sea ice extent decreases, this will lead to more absorption of solar energy and thus affect global climate change.

From the regional perspective, seasonal sea ice variance affects the local ecological cycle and human economic activities. Sea ice can release nutrients when it melts, and the vertical convection of seawater caused by ice freeze can bring the nutrients from the bottom of the sea to the surface [4]. The delivery of these nutrients nourishes many marine organisms. In addition, many polar mammals choose sea ice as their habitat. The variation of sea ice extent affects the population of these animals. In terms of socio-economic perspectives, sea ice floes cannot be ignored in polar navigation and offshore activities, such as fisheries, aquaculture, global shipping, and oil and gas exploration and production (EP) [6]. A key requirement for these activities is providing detailed, synoptic, and timely information on sea ice, including distribution and a variety of physical characteristics [7].

Since the 1970s, the average combined land and ocean surface temperature increased by 0.85 °C [3], which led to the global mean sea level increasing by 0.2 meters, and the Arctic sea ice extent decreased by 3.5–4.1% per decade [3]. The rapidly changing cryosphere environment could negatively affect the climate, biology, and socio-economic activities. As a result, the motivation for sea ice monitoring shifted from being military and offshore industry-driven to being environmentally driven [8].

Sea ice can be discriminated into a variety of types in terms of different characteristics, such as age, salinity, porosity, and surface roughness. According to the World Meteorological Organization (WMO) definition [1], sea ice types can be defined according to their development stage. Ice that is recently formed and composed of crystals is new ice, which includes frazil ice, grease ice, slush and shuga. The next stage is nilas, a thin elastic ice crust which easily bends on ocean waves. Young ice is an intermediate stage between nilas and first-year ice; it can be subdivided into grey ice and grey-white ice. First-year ice is the ice developed from young ice and of not more than one winter's growth. It can be subdivided into thin, medium and thick first-year ice. Ice that has survived more than one summer's melt is multi-year ice. More multi-year ice survives in the Arctic than in the Antarctic. Sea ice monitoring consists of several applications, such as ice type classification [9–13], sea ice extent detection [14, 15], ice concentration [16–20] and ice thickness [21–25] estimation, and ice drift (or motion) retrieval [26–30]. Ice motion retrieval is fundamental for the determination of ice transport rate, ice flow dynamics analysis, and the investigation of the driving force behind ice flow change [3]. Sea ice extent is conducive to investigating factors that influence annual sea ice changes. For example, the change of sea ice extent responds early to climate change caused by greenhouse gases [5]. Sea ice thickness is useful for understanding mass/volume, heat, and salt fluxes, which are essential for global climate change study. Sea ice classification is considered one of the most important tasks for sea ice charting among these applications. The spatial distribution and areal fraction of different ice types are required for future global climate estimation [31]. Furthermore, classification results can be used as an intermediate input to obtain other sea ice parameters, such as sea ice concentration and extent [32].

Field exploration of sea ice is dangerous and time-consuming, and the obtained sea ice data are also limited in spatial coverage [33]. Due to the broad coverage, the extremely harsh environment in the polar regions, and the near real-time requirements of some applications, remote sensing has become one of the main techniques for sea ice monitoring. Conventional sea ice monitoring methods include ice buoys [34], in-situ ship observation [35], shore-based radar [36], and airborne lidar [37]. However, these methods are impractical for frequent and large-scale sea ice monitoring [3]. In addition, the extent of sea ice changes with the seasons, and floating ice also moves with the ocean current [3]. That means monthly or weekly sea ice charting is required in a vast region. Therefore, a reliable tool that frequently monitors sea ice on a global scale is demanded. As an alternative, satellite sensors provide a more efficient and cost-effective method for sea ice monitoring. These sensors operate in different spectrum ranges (optical, infrared, and microwave (passive and active)) and provide information at different scales [8]. To discriminate between sea ice and open water, optical sensors are based on albedo contrast, thermal infrared sensors focus on physical temperature difference, and microwave sensors utilize the difference of microwave emissivity [8]. Many techniques have been developed using these sensors to retrieve sea ice parameters. For instance, the surface temperature can be retrieved from thermal infrared sensors, ice concentration and extent can be estimated from passive microwave sensors, and ice types can be discriminated from passive and active microwave sensors [7]. Although sea ice parameters can be measured by various sensors, there are still several challenges in sea ice observations. Passive microwave radar suffers coarse spatial resolution [38]. Applications of optical sensors and thermal infrared sensors are also limited by environments. Synthetic Aperture Radar (SAR) interacts with sea ice at the macroscopic level and collects sea ice properties, such as structure and surface roughness [31]. For objects' illumination, SAR sensors only rely on their radiation sources. Moreover, the SAR sensor can penetrate clouds, dry ice cover and snow due to its long wavelength [39]. Self illumination and long wavelength lead to its all-weather, day-and-night imaging capability with high spatial resolution [40]. Due to these advantages over other types of sensors, SARs can be used for validating coarse resolution results from radiometers and scatterometers, as well as achieving better descriptions of regional ice distributions [31].

Satellite SARs can be used to monitor the evolution of microwave scattering signatures of sea ice. The intensity of each pixel in SAR images is usually expressed as the normalized radar cross-section (NRCS), denoted as σ^0, with units of dB. The physical and thermodynamic state of sea ice can be represented as a collection of its dielectric properties, which affect the microwave interactions with sea ice [41]. SAR backscattering signature (signal intensity and phase) for sea ice is mainly determined by small-scale ice and snow characteristics and by ice salinity and temperature [31]. Therefore, to retrieve different sea ice types from SAR data, the main goal is to investigate the relationship between sea ice types and SAR backscattering characteristics of small-scale sea ice properties in different environmental conditions [31]. Surface scattering and volume scattering are the main interactions between SAR waves and sea ice. When a SAR illuminates a surface smoother than its wavelength, it shows specular reflection characteristics, and the surface scattering is dominant. The regions like nilas and young ice will appear dark in SAR images [31]. Volume scattering occurs when microwaves penetrate sea ice and are reflected by the volume inclusions (such as bubbles and brine pockets) in the sea ice. As the radar frequency, ice salinity and temperature increase, the microwave penetration depth decreases [31]. For linear polarization, HH (horizontal co-polarization) generally provides information about the surface scattering of the sea ice, while HV (cross-polarization) mainly provides information about volume scattering. For example, co-polarization intensity (σ^0_{hh} and σ^0_{vv}) increases with the initial growth of sea ice thickness; however, co-polarization ratio ($\sigma^0_{vv}/\sigma^0_{hh}$) decreases with the increase of thin ice thickness [42].

The surface scattering and volume scattering of various ice types by SAR sensors are affected by ice surface roughness, salinity, porosity, etc. [31]. Using thresholds or empirical formulas based on SAR data are straightforward methods for sea ice classification. However, these techniques may be only applicable for the selected dataset [8]. What's more, the overlap of backscattering signatures of different sea ice types leads to the difficulty of realizing accurate and robust sea ice classification. As an alternative, machine learning technology based on large data sets can achieve automatic and powerful applications. The effective throughput of the trained model makes it possible to apply near-real-time sea ice classification and can assist ice experts' analysis more conveniently [41].

1.2 Sea Ice Classification Background

A continuous and nearly complete record of global sea ice cover had not been available until the launch of the SEASAT satellite in 1978, followed by Kosmos-1870 (1987) and Almaz-1 (1991) [43]. These early satellites carrying SAR sensors showed the potential of SAR for sea ice monitoring. ERS-1 and ERS-2, launched by the European Space Agency (ESA) in 1991 and 1995 for sea ice mapping and ship navigation, became a significant milestone in spaceborne SAR sea ice sensing, due to their continuous service of more than 10 years, delivering tens of thousands of SAR sea ice images across the world [44]. However, their low swath width limited their spatial coverage and their usage in operational monitoring [43]. In 1992, the National Space Development Agency of Japan (NASDA) launched JERS-1, which carried an L-band SAR sensor. The longer wavelength of the L-band and shallow incidence angle of JERS-1 made it more qualified for detecting ridges, rubble fields, brash ice and other ice surface deformation than the C-band SARs [44]. In 1995, RADARSAT-1, launched by the Canadian Space Agency (CSA), overcame the shortage (limited resolution and coverage) of previous SARs and provided satellite images with multiple SAR imaging modes. It became one of the primary data sources of national ice service centers in several northern countries. Ice area and volume production can be estimated based on sea ice deformation fields and linear kinematics features derived from RADARSAT-1 ScanSAR images [44]. However, RADARSAT-1 only provided a single polarization mode (HH). Such imagery is limited by its inability to discriminate between certain ice types and open water states. A single polarization channel alone could be insufficient for some sea ice sensing applications. Therefore, texture features or advanced segmentation techniques were employed to obtain optimal classification results. For example, weighted gray-level co-occurring probabilities (WGLCP) were compared with gray-level co-occurring probabilities (GLCP) in [45] for the classification of ice and water. According to [46], water and sea ice types can be classified based on iterative region growing using semantics (IRGS) for segmentation and the Markov random field (MRF) method for region-based classification.

Sea ice classification was further improved with the development of multi-polarization radar technology between the end of the 20th century and the beginning of the 21st century. SIR-C/X-SAR is a short-term mission. Its system was integrated into the space shuttle with two flights from 9 to 20 April and 30 September to 11 October 1994. The SIR-C radar beam was capable of providing four polarization combinations: HH, VV, HV, and VH. Compared to single-polarization images (HH or VV), the increased information content from the introduction of cross-polarization channels (HV and VH) can enhance the accuracy of sea ice observation. After the launch of ENVISAT in 2002, many multi-polarized radars of different bands were developed, such as the C-band RADARSAT-2 (2007, CSA), the X-band TerraSAR-X and TanDEM-X (2007 and 2010, German Aerospace Center), the L-band ALOS and ALOS-2 (2006 and 2014, Japan Aerospace Exploration Agency), the X-band KOMPSAT-5 (2013, Korea Aerospace Research Institute), the C-band Sentinel-1 A/B (2014 and 2016, European Space Agency) and the C-band Gaofen-3 (2016, China National Space Administration). Decomposition feature analysis of RADARSAT-2 quad-polarized data was conducted in [47], where σ^0_{hh}, σ^0_{vv}, the total power and surface scattering component, were analyzed with a wider range of environmental conditions. As investigated in [48], sea ice classification performances were compared among L-, C- and X- band SARs. It was discovered that the C-band is more robust for sea ice classification in general, but the X-band and the L-band can distinguish several specific sea ice types better. For example, L-bands provide better discrimination between young ice and smooth first-year ice compared with the C-band since the correlation coefficient of the L-band was observed to be a vital feature for the discrimination of young ice and smooth first-year ice. In addition, sea ice observation using multi-frequency SARs is also analyzed in [49, 50]. In [49], L-band SAR was found to be able to identify ice ridges more easily because longer wavelength data are less affected by microscale ice structures. The work presented in [50] showed that X-band SAR can easily discriminate newly formed sea ice from open water due to its lower penetration depth. Although the additional information contained in the quad-polarization (HH, VV, HV, and VH) mode of SAR imagery can be used to improve sea ice sensing applications, current image swath widths (up to 50km for RADARSAT-2 quad-polarization) are too small for the requirement of large-scale sea ice monitoring [51].

Nowadays, coherent dual-polarization imaging mode is considered a critical choice instead of conventional linear polarization modes. Hybrid compact polarization (HCP) transmits a right-circular polarization. It receives two mutually coherent orthogonal linear polarizations (RH and RV), offering more information than dual-polarization mode, while covering much greater swath widths compared to quad-polarization mode [40]. The first two HCP missions (India's Chandrayaan-1 (CH-1) and NASA's Lunar Reconnaissance Orbiter (LRO)) are used for moon observation [52, 53]. Three earth observation missions (India's RISAT-1 (2012), Japan's ALOS-2 (2014), and Argentina's SAOCOM (2018) with experimental HCP capabilities) were launched later. Among them, RISAT-1's HCP data became one of its most popular and successful products [54]. The RADARSAT Constellation Mission (RCM), launched on June 12, 2019, provides quad-polarization mode as well as HCP configuration. Nearly polarimetric data have been available for the first time from the ScanSAR mode of RCM [44], bringing significant progress to enable large-scale and accurate sea ice classification in the future. Most research on RCM is based on simulation data rather real RCM data. HCP features decomposition was carried out in [55]. It showed promising results for ice classification and may have a similar classification potential compared with that of the quad-polarization mode. In another study [56], 26 HCP features based on the Kolmogorov-Smirnov test in different seasons and incident angle ranges were analyzed. It was found that the phase difference between σ^0_{RH} and σ^0_{RV}, the third Stokes vector, m-chi-even-bounce and the compact polarimetry parameter alpha provide useful discrimination among different sea ice sub-types.

1.3 Motivation and Objectives

RADARSAT-2 and Sentinel-1 have been widely applied for sea ice classification as open-access satellite platforms providing multi-polarized C-band SAR data. RCM is a new generation of RADARSAT missions offering traditional multi-polarization modes like RADARSAT-2 as well as HCP configuration. Because RCM was launched only recently, most studies on HCP mode are based on simulation data using quad-polarized RADARSAT-2 images [57]. The applicability of different satellite platforms (including Radarsat-2, Sentinel-1 and RCM) was analyzed in [58, 59] for landslide monitoring. The authors emphasized the RCM advantages of a shorter revisit time and higher spatial resolution for the detection of small-sized slope movements, compared with previous SAR satellites. In [60], a large number of Sentinel-1 and RCM images were combined to generate the sea ice motion product across the Arctic, which provides more sea ice vectors in summer with higher spatial coverage and temporal resolution compared with that of previous sea ice motion products (e.g., National Snow and Ice Data Center Polar Pathfinder and the Ocean and Sea Ice-Satellite Application Facility). In [39], RCM compact polarization channels (CH, CV) were compared with the linear polarization channels (HH, HV) of RADARSAT-2 and Sentinel-1 in terms of river ice classification. In that study, ground range detected (GRD) compact polarization data are used, and gray-level co-occurrence matrix (GLCM) texture features are extracted for river ice classification. The superiority of the compact polarimetry mode over linear polarimetry is demonstrated in [39, 43]. A new ice concentration algorithm using dual-polarized RCM data with derived ocean surface wind speed was developed in [61]. The root-mean-square error of this new ice algorithm can reach 2.2%, and its R^2 is 0.997. It should be noted that there are no studies for sea ice classification using real RCM images or comparing the sea ice classification performance of RCM with other C-band SAR missions.

The surface scattering and volume scattering of various ice types by SAR sensors are affected by ice surface roughness, salinity, porosity, etc. [31]. This leads to the feasibility of machine-learning-based sea ice classification. Machine learning technology based on large data sets can achieve automatic sea ice charting. The robust throughput of the trained model makes it possible to realize near-real-time sea ice monitoring and facilitate analysis by ice experts [41]. Conventional machine learning algorithms, such as support vector machine (SVM) and random forest (RF), have been widely adopted since they are easy to use and do not require much training data but can obtain a high accuracy [3]. Usually, RF is preferred among those conventional methods because it is based on ensemble techniques, which collect weak learners to reduce variance while maintaining low bias. However, conventional approaches may not work well for some new ice types, such as new ice [62], gray ice [63] and young ice [64]. The sliding bagging ensemble SVM, refined with first-order logic, was presented in [63] for sea ice classification using dual-polarized RADARSAT-2 data. Its demonstrated accuracy for gray ice was only 52.2%. A locality-preserving fusion technique for multi-source images was developed in [65]; the sliding bagging SVM trained using the fusion dataset from multi-spectral and SAR images can achieve an overall accuracy of 94.11%. In [66], the authors classified melt pond, sea ice and water using RF and decision trees (DT) and found that RF was superior to DT and HH. Moreover, the spatial standard deviation, the average of the co-polarization phase differences and the alpha angles were effective features for the RF model. In [67], an optimized DT that splits multi-class classification problems into binary problems at each branch showed an improvement over the traditional all-at-once classification algorithm and its results were comparable to those of the commonly used RF approach. Park et al. [64] applied RF with GLCM parameters to Sentinel-1 data for the classification of open water, mixed first-year ice and old ice and achieved an overall accuracy of 87%. Meanwhile, deep convolutional neural networks (CNNs), which consist of tens to hundreds of layers and can be trained using the residual learning technique, have also been employed in sea ice monitoring applications, such as classification [41] and concentration estimation [68]. CNNs can replace complicated feature engineering procedures with simple end-to-end deep learning workflows by extracting spectral and spatial information based on their multi-layered interconnected channels [69]. The technique based on deep neural network usually performs better than the traditional machine learning technology under the same conditions [70, 71], but it also requires a large amount of training data and time. Although deep CNNs have the potential to provide more accurate results for sea ice monitoring, it should be noted that deep CNNs are also limited by the intricate tuning process, heavy computational burden, the high tendency of overfitting and the empirical nature of model establishment [69]. For sea ice classification, the availability of a large number of accurately labeled data is also a challenge [41]. In [72], a state-of-the-art CNN, Visual Geometric Group–16 Layer (VGG-16), that can classify five cover types (water, brash/pancake ice, young ice, level first-year ice and deformed ice) with the highest overall accuracy of 99.89% is proposed. Unlike traditional sequential CNN architectures (e.g., VGG), the residual neural network (ResNet) [73] is a network-in-network architecture consisting of micro-architecture building blocks (also called residual blocks). Residual blocks are realized by adding skip connections to avoid vanishing gradients and mitigate the problem of degradation (accuracy saturation). As a result, extremely deep networks can be effectively trained. The first residual network (ResNet-50) was introduced by He et al. [73] in 2015. Its top-1 accuracy in ImageNet was 2.75% higher than that of VGG-16 [74]. Normalizer-Free ResNet (NFNet) [75] is a new family of ResNet classifiers released by the DeepMind company that achieved a new state-of-the-art accuracy on the ImageNet dataset. Many deep CNNs rely heavily on batch normalization as a critical component, whereas NFNets improve training speed by replacing batch normalization with the adaptive gradient clipping (ADC) technique. In this study, the feasibility of NFNets for sea ice classification is investigated. This state-of-the-art technique (NFNet) is also compared with the RF method in sea ice classification using RCM data.

The difference between manually drawn ice charts and automatic ice charts is discussed in [76]. Manually drawn ice charts are affected by the education and experience of the ice analysts. Even using the same data source, different ice experts may produce different sea ice charts. Moreover, manually drawn ice charts show rough boundaries and relatively poor detail, whereas automatic ice charts can help to interpret image information more rigorously and distinguish more segments. In the traditional manual production of weekly regional ice charts, their main data sources are satellite images, as well as corresponding daily ice analysis charts [1]. The ice charts are manually drawn directly by ice experts using geographic information systems (GIS) software. However, it is time-consuming for ice experts to analyze many satellite images, and pixel-level classification is impossible. In contrast, once the machine-learning-based classifiers are trained properly using a data set with a sufficient amount and diversity, near real-time classified results can be generated, and pixel-level classification can be achieved. In this study, the classified results can also be used to estimate the concentration in a region with a specific value rather than a rough concentration code.

1.4 The Scope of the Thesis

In this thesis, RCM data are utilized for sea ice detection and classification using NFNet for the first time. The thesis is organized as follows:

In Chapter 2, HH, HV and the cross-polarization ratio are extracted from the dual-polarized RCM data with a medium resolution (50 m) for an NFNet-F0 model. A two-level random forest (RF) classification model is also applied as a conventional technique for comparisons with NFNet. The sea ice concentration estimated based on the classification result from each region is validated with the corresponding polygon of the Canadian weekly regional ice chart.

In Chapter 3, sea ice classification results of the two C-band SAR missions with the state-of-the-art convolutional neural network, NFNet, are compared. HH, HV and cross-polarization ratio are extracted from the overlapping area of dual-polarized RCM and Sentinel-1 images acquired on similar dates.

The summary of the thesis and suggestions for future work are outlined in Chapter 4.

The achievements of this research have been published as follows:

1. H. Lyu, W. Huang, and M. Mahdianpari, "A meta-analysis of sea ice monitoring using spaceborne polarimetric SAR: advances in the last decade," *IEEE J. Sel. Top. Appl. Earth Obs. Remote Sens.*, vol. 15, pp. 6158-6179, July 2022.

2. H. Lyu, W. Huang, and M. Mahdianpari, "Eastern Arctic sea ice sensing: first results from the RADARSAT Constellation Mission data," *Remote Sens.*, vol. 14, no. 5, pp. 1165, Feb. 2022.

3. H. Lyu, W. Huang, and M. Mahdianpari, "Sea ice detection from the RADARSAT Constellation Mission experiment data," in *Proc. IEEE 34th Can. Conf. Electr. Comput. Eng.*, ON, Canada, Sept. 2021, pp. 1-4.

4. H. Lyu, W. Huang, and M. Mahdianpari, "NFNet based sea ice classification from RADARSAT Constellation Mission data," in *Proc. 43rd Can. Symp. Remote Sens.*, Quebec, Canada, July 2022, pp. 1-4.

5. H. Lyu, and W. Huang, "Comparison of sea ice classification from RCM and Sentinel-1 SAR imagery," in *Proc. IEEE 42nd Int. Geosci. Remote Sens. Symp.*, Kuala Lumpur, Malaysia, July 2022.

Among the 5 published articles, some contents of Chapter 1 come from article 1, the contents of articles 2, 3 and 4 are associated with Chapter 2, and Chapter 3 is based on article 5.

Chapter 2

Eastern Arctic Sea Ice Sensing: First Results From the RADARSAT Constellation Mission Data

This chapter which comes from [77–79][1] provides the first sea ice detection and classification results from real dual-polarized RCM data. The feasibility of NFNets for sea ice classification is investigated. This technique (NFNet) is also compared with the RF method in sea ice classification using the RCM data. The chapter is organized as follows. The RCM and ground truth data are described in Section 2.1. The methodology used for RCM sea ice

[1] [77] H. Lyu, W. Huang, and M. Mahdianpari, "Eastern Arctic sea ice sensing: first results from the RADARSAT Constellation Mission data," *Remote Sens.*, vol. 14, no. 5, pp. 1165, Feb. 2022.

[78] H. Lyu, W. Huang, and M. Mahdianpari, "NFNet based sea ice classification from RADARSAT Constellation Mission data," in *Proc. 43rd Can. Symp. Remote Sens.*, Quebec, Canada, July 2022, pp. 1-4.

[79] H. Lyu, W. Huang, and M. Mahdianpari, "Sea ice detection from the RADARSAT Constellation Mission experiment data," in *Proc. IEEE 34th Can. Conf. Electr. Comput. Eng.*, ON, Canada, Sept. 2021, pp. 1-4.

Author Contributions: All authors made substantial contributions to the conception and the design of the study. H.L. performed the experiments. W.H. and H.L. analyzed the data and wrote the paper. All authors reviewed and commented on the manuscript.

classification in this study is explained in Section 2.2. Experiment results are presented and discussed in Sections 2.3 and 2.4, respectively. Section **??** summarizes the classification processes and outlines suggestions for future investigations.

2.1 Study Area and Data Set

2.1.1 Study Area

This chapter presents a case study of the Davis Strait. The investigation area was close to Buffin Island in the Canadian Arctic. Under the effects of different water masses and ocean currents, the sea ice in the Davis Strait displays strong seasonal variation that has a further influence on local light, stratification, nutrient availability, and temperature [2]. Despite the decrease in global sea ice in the past 25 years, the sea ice coverage in this area has increased [2]. In general, sea ice appears at the Davis Strait in mid-October and its extent reaches the maximum value in March [6]. From late July to early August, the ice thickness and coverage rapidly decrease to an ice-free state [6]. At the acquisition times (21:21 (UTC) January 4, 21:29 (UTC) March 1 and 22:11 (UTC) March 2) of the RCM images used in this study, the mean air temperature was around -24 °C to -25 °C , and air temperature was below 0 °C for several months. However, since this area is well known for its available fisheries and rich oil and gas resources, the presence of sea ice poses a serious threat to the local economy [2]. Therefore, near real-time sea ice detection and mapping is of great significance to local economic activities.

2.1.2 Sea Ice Chart

In many countries, sea ice charts are provided by their national ice service centers (such as Canada, the USA, Russia, etc.) as the main source of sea ice information. Sea ice charting is based on geographic information system technology, which requires all available satellite data, as well as in situ visual observations and manual labels applied by ice experts.

The spatial resolution of the satellite data source used for the Canadian Ice Service (CIS) regional ice chart ranges from a few tens of meters to a few kilometers [1]. Although the CIS also provides daily ice charts, the daily data for the areas under investigation are not available. In this study, the temporal resolution of the digital ice chart (shapefile format) obtained from CIS was one week. Thus, the sea ice distribution information may not be precise, bringing significant challenges to the labeling strategy for training. Because the temporal and spatial resolutions of the sea ice chart are different from those of RCM data, the sea ice chart cannot be used for labeling each RCM pixel directly but for generating manual labels via interpolation only for homogeneous areas with only ice or water. In this way, an effect on the classification results may exist but should not be significant. Manual selection of uniform areas can partially mitigate the error of the sea ice chart. On the sea ice chart, each ice region is associated with one egg code, containing the information about sea ice concentrations, stages of development (age) and the form (floe size) of ice. In this study, we focus on the stage of development and sea ice concentration. The abbreviations for each type of ice are shown in Table 2.1. For this study, the sea ice types were mainly first-year ice, gray white ice and gray ice. Only few regions contained old ice (OI), so old ice was not considered separately but was combined with first-year ice (FYI) and classified as OI/FYI. Gray white ice, gray ice and new ice were combined under the category of new ice (NI) because they are reported in the same sea ice chart polygons. The sea ice concentration code represents the percentage of ice coverage of an area in tenths. Note that the region with a concentration less than 10% is labeled as ice-free, open water and bergy water. A concentration code of "10" indicates consolidated ice. In this study, two (January 4 and March 1 ice charts) weekly regional ice charts in shapefiles from the Canadian Ice Service were used as reference for labeling. A shapefile of a sea ice chart is a georeferenced digital chart consisting of polygons, each of which contains an attribute that describes its sea ice information in detail.

Table 2.1: Sea ice types and the corresponding stage of development (age) egg codes [1].

Description	**Abbreviation**	**Thickness**	**Code**
New ice	NI	<10 centimetres	1
Grey ice	GI	10 - 15 centimetres	4
Grey-white ice	GWI	15 - 30 centimetres	5
First-year ice	FYI	>=30 centimetres	6
Thin first-year ice	TFYI	30 - 70 centimetres	7
Medium first-year ice	MFYI	70 - 120 centimetres	1·
Thick first-year ice	TKFYI	>120 centimetres	4·
Old ice	OI	-	7·

Table 2.2: Characteristics of RCM imagery used in this study.

Attributes	**1st RCM Image**	**2nd RCM Image**	**3rd RCM Image**
Time	2021/3/1	2021/3/2	2021/1/4
Satellite	RCM-3	RCM-2	RCM-1
Beam Mode	Medium Resolution 50m		
Pixel Spacing	20m		
Polarizations	HH HV		
Incidence Angle	26.85°- 50.90°	34.07°- 55.08°	26.87°- 50.96°
Spatial Coverage	384.88km × 362.46km	570.64km × 363.94km	564.06km× 363.3km
Latitude	64.57N - 68.55N	67.87N - 73.47N	63.31N - 68.9N
Longitude	55.19W - 64.98W	64.14W - 76.84W	54.77W - 65.22W

2.1.3 RCM Data and Sea State Information

Three dual-polarized images, acquired on 4 January and 1 and 2 March 2021, were used and these are shown in Figures 2.1 (a) and (c). The information on the RCM images is summarized in Table 2.2. Sea ice classification can be affected by sea state conditions [48,80]. ERA5 [81] can provide global hourly ocean wave estimates based on reanalysis that combines physical models with observations from ground sensors and satellites, such as ERS-1, ERS-2 and Envisat. The stars in Figures 2.1 (a) and (c) display the locations where the sea state information from ERA5 is used. At the acquisition time of the March 1st image around the Davis Strait, the significant wave height was 1.5 m, the period was 5.1 s and the direction was 173.3°. On March 2nd, the significant wave height was 2.1 m, the period was 6.7 s and the direction was 176.6°. The yellow star on January 4th is close to the NI testing samples, where the significant wave height was 1.7 m, the period was 5.3 s and the direction was 241.3°. The red star in Figure 2.1 (c) is located near the water testing samples, where

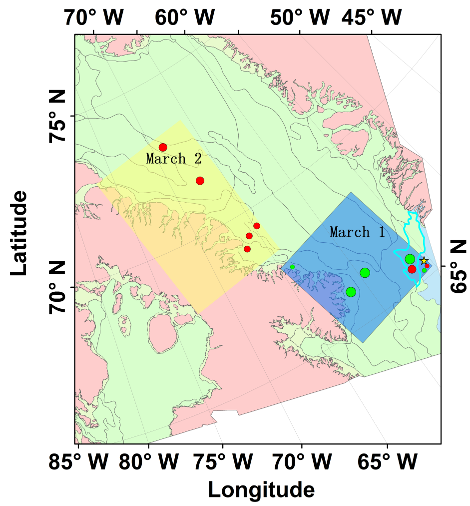

(**a**) March 1 and 2 images.

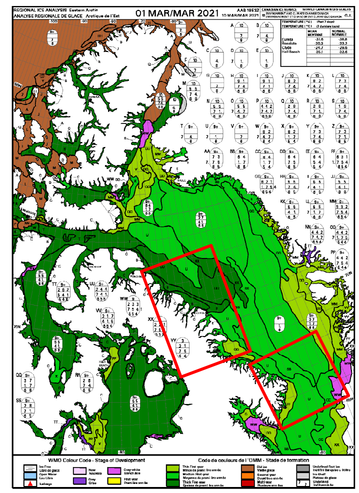

(**b**) Sea ice chart (March 1).

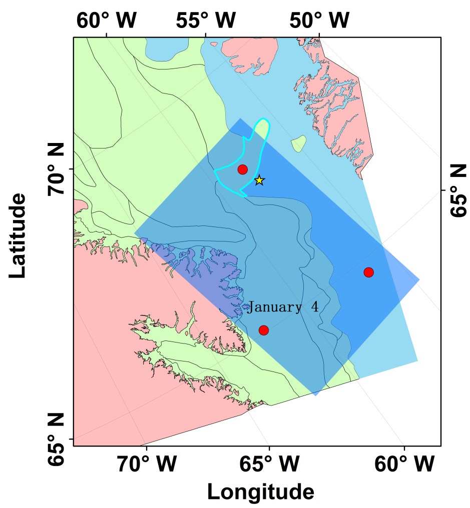

(**c**) January 4 image.

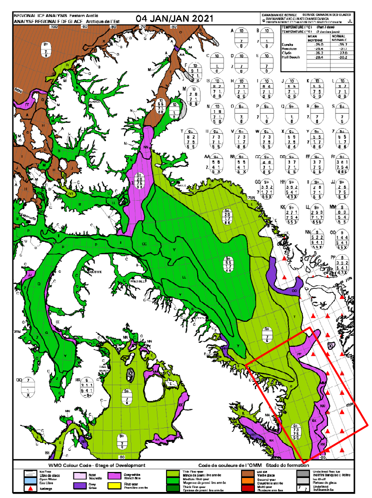

(**d**) Sea ice chart (January 4).

Figure 2.1: (**a**) The March 1st and 2nd RCM images laid over sea ice charts. Light green represents ice, light blue represents water and pink represents land. The yellow star represents the location with sea-state information. The March 1st image was used for selecting training samples, and the first testing set samples of NI and water. The March 2nd image was used for selecting the first testing set samples of OI/FYI. Green dots indicate the locations for selecting the training samples. Red dots indicate the locations for choosing the testing samples. (**b**) Regional sea ice chart in the Eastern Arctic for the week of March 1st 2021. Red rectangles indicate the coverages of the March 1st and 2nd RCM images. (**c**) The January 4th RCM image laid over a sea ice chart (color codes are same as those in (**a**)). The stars are the locations with sea-state information near the testing samples. The January 4th image was used for selecting the second testing set samples. Red dots also indicate the locations where the testing samples were collected. (**d**) Regional sea ice chart in the Eastern Arctic for the week of January 4th 2021. The red rectangle illustrates the coverage of the January 4th RCM image.

the significant wave height was 1.5 m, the period was 5.7 s and the direction was 219.5°. According to the World Meteorological Organization (WMO) code [82], the sea states at the acquisition times of the three RCM images are moderate. Therefore, the training set and testing set were collected under similar sea-state conditions.

2.1.4 Training and Validation Datasets

In order to obtain reliable sea ice samples from the RCM data based on the digital sea ice chart to train a machine-learning-based classifier and evaluate its performance, a reasonable labeling strategy is required. Labeling is divided into two steps: automatic labeling and manual labeling. Automatic labelling was only applied to generate the corresponding sea ice chart of an RCM image. The homogeneous regions were manually selected and labelled according to the sea ice charts. Then, training and testing samples were randomly selected from those manually labelled homogeneous regions. For the georeferenced RCM image, the longitude and latitude of each pixel are known, so the georeferenced coordinates are firstly converted into the Lambert Conic Conformal−Two Standard Parallels (2SP) projection format to match the projection mode of the digital sea ice chart. The sea ice chart polygon to which each pixel belongs can be determined. By reading the attribute of the corresponding polygon from the digital sea ice chart, each pixel's egg code can be acquired. In this way, the initial automatic labeling can be realized. However, the sea ice chart cannot indicate specific sea ice information for each pixel, but rather for a polygon. In a polygon with a low sea ice concentration, the ice and water distribution is not specified. If the machine learning model is trained directly according to the automatically labeled pixels, a large number of pixels corresponding to water will be misclassified as ice. Therefore, manual labeling is required to generate more accurate training and testing samples.

In this study, only homogeneous areas completely covered by sea ice or water were selected for manual labeling. Next, inside these regions, only those parts that also look like ice in the RCM images were finally selected as training samples. Similar steps but with a concentration lower than 10% were used for the selection of water samples. Here, only three classification types are considered. Ice with a stage of development code of new ice to gray-white ice is labeled as NI, that with the code of first-year ice to old ice is labeled as old ice and first-year ice (OI/FYI, see Table 2.1). Considering that the polygons used for selecting the NI samples (illustrated in Figures 2.1 (a) and (c) with blue borders) contain some other cover types, only the areas displayed as clearly bright in the pseudo-color images were used for the selection of the NI samples. The green and red dots indicate the locations for selecting the training and testing samples, respectively. These locations were chosen since each of them belongs to a large homogeneous area. Ice-free, open water and bergy water are labeled as water. Bergy water and open water both represent areas where the sea ice concentration is less than 10%. For this data set, the ice in bergy water was mostly glacier ice. Ten thousand training samples were selected from the March 1 image for each class.

In this study, two testing sets were adopted. For the first testing set, ten-thousand OI/FYI samples were obtained from the March 2nd image, whereas ten-thousand NI and ten-thousand water testing samples were obtained from the March 1st image and 10 km away from the training samples, since the March 2nd one rarely contained these two types. The March 1st image rarely contained NI and water because the March 2nd image is located inside the sea ice area. The region for selecting new-ice testing samples is highlighted with a blue border (see Figure 2.1 (a)). The first testing set was from March 1st and March 2nd, and both days shared the same sea ice chart. Little variation in sea ice condition was expected between these two days since the time difference was only one day. To further evaluate the generalization ability of the two classifiers through testing samples from different times and locations, the samples for the second testing set were only selected from the January 4th image and far away from the training samples in the March 1st image. For the second testing set, the OI/FYI and water testing samples were selected from the south portion of the January 4th image and more than 100 km away from the corresponding training samples. The NI samples of the second testing set were from the polygon outlined with a blue line in Figure 2.1 (c). Although some other regions in the January 4th image also contained NI, the highlighted area in Figure 2.1 (c) was the farthest (more than 172 km) from the training samples. Because the NI samples of the training set only came from one polygon of the sea ice chart and the NI samples of the training set were different from that of the testing set in terms of both time and location, it could have been difficult for the classifiers to distinguish NI from other cover types. From another perspective, the NI classification results can also be utilized to compare the two models' generalization ability.

The confusion matrix, kappa coefficient, F1-score and overall accuracy were used to evaluate the classification performance based on those testing samples. The total sea ice concentration statistics and the distribution percentages of different sea ice types in different areas were calculated and compared with the egg codes from the digital sea ice charts. The total concentration and distribution percentage can be determined by dividing the number of pixels of the corresponding ice type by the total number of pixels excluding land in a region. If an area contains land, the land is labeled via a land mask image. These land pixels are not involved in further analysis, including concentration and distribution calculations.

2.2 Methodology

2.2.1 Preprocessing

SAR data need to be preprocessed to enhance the data quality and meet different application requirements, for example, mitigating the noise from reflection and geometric distortion caused by terrain changes. Figure 2.2 displays the preprocessing steps for dual-polarized RCM images. The Sentinel Application Platform (SNAP) [83], developed by the European Space Agency (ESA), contains various free open source toolboxes for earth observation missions. In this paper, SNAP was employed to implement most preprocessing steps except destriping.

First, calibration was accomplished by converting two digital channels (HH, HV) of

Figure 2.2: RCM preprocessing steps.

the RCM data into the backscattering coefficient σ^0 in decibels, which indicates the target backscatter properties, according to [84]:

$$\sigma^0 = \frac{D^2 + B}{A} \tag{2.1}$$

$$\sigma^0(\text{dB}) = 10\log_{10}(\sigma^0) \tag{2.2}$$

where B is the offset and A is the range dependent gain value that can be found in the RCM metadata file, D is the digital value for each pixel from the RCM tiff file.

For speckle filtering, the improved Lee sigma filter with a square window size of 7 by 7 was adopted [85]. This filter was modified from the Lee sigma filter by reducing the bias caused by asymmetric Rayleigh distribution, unfiltered black pixels and the smearing of strong targets [85]. In this study, a window with a side length of 7 was selected because it can achieve effective speckle filtering while maintaining more texture information [85].

Thermal noise is an additive background energy, and it varies along both the range and azimuth axes and is exhibited as alternating extraordinarily bright or dark stripes in SAR images [86]. In addition to conventional SAR preprocessing steps, destriping is implemented as an extra step between speckle filtering and geocoding since thermal noise can significantly affect pixel-based sea ice classification. Note that the thermal noise in the HV channel is more evident than the HH channel in a linear polarized SAR image. Thus, destriping is only applied to the RCM HV channel here. Destriping is applied to each pixel of the RCM HV channel through subtracting an intensity offset and then dividing by a gain factor [87]. Figures 2.3 (a) and (c) illustrate the images before and after applying destriping. As can be seen, the stripes of the HV channel are partially successfully removed after destriping. As shown in Figure 2.3 (b), ten-thousand samples for each class are used for training in this example. The blue pixels in the large green region are thermal noise and they are classified as water if destriping is not applied, but are classified correctly in Figure 2.3 (d).

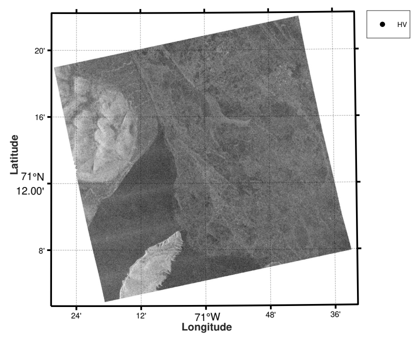

(**a**) Before destriping.

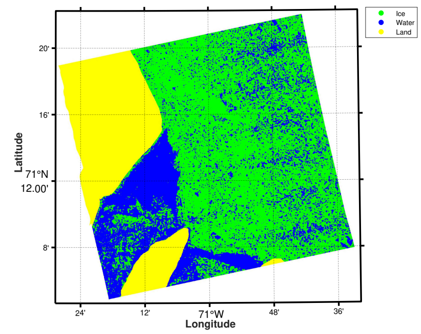

(**b**) Result without destriping.

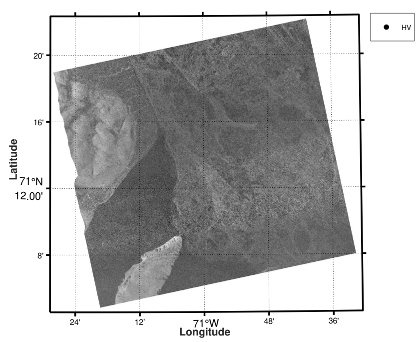

(**c**) After destriping.

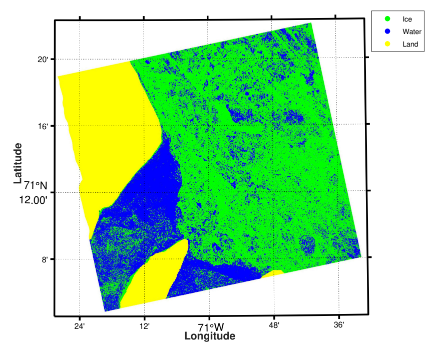

(**d**) Result with destriping.

Figure 2.3: Destriping examples. Image acquired on 2 March 2021.

Geocoding is implemented via range doppler terrain correction, which uses available orbit state vector information, the radar timing annotations, the slant-to-ground range conversion parameters in the metadata file with the reference Digital Elevation Model (DEM) data to derive the precise geolocation information [88]. The most commonly used DEM is SRTM, which only provides high-precision elevation data below 60 °N. The study area is over 60 °N, so Copernicus DEM GLO-30 was selected for geocoding because it provides global elevation data with a 30 m resolution. To realize automatic labeling as described in the last section, Lambert Conformal Conic 2SP was used for map projection, of which the projection parameters are consistent with the digital sea ice chart. Finally, land regions were masked out according to the DEM in order to avoid false labeling.

The σ^0 value changes with the incidence angle for ice type, season, and radar frequency [64, 89, 90]. Most papers that consider incidence angle variability employ universal linear correction, which is based on an empirical linear relationship between mean sea ice backscattering and incidence angle value. Such a correction usually requires the sea ice type information to be known in advance. However, the ice types were known not for all the pixels in the preprocessing step. Whether considering incidence angles variability in sea ice application is good or not is still a problem under investigation. The incidence angle variability was ignored in this study. The influence of incidence angle on the NFNet model will be investigated in future research.

2.2.2 Normalizer-Free ResNet

2.2.2.1 Normalizer-Free ResNet Architecture

The NFNets were realized based on the SE-ResNeXt-D model with Gaussian error linear unit (GELU) activations here, and its structure is displayed in Figure 2.4. GELU activation layers were omitted between convolutional layers. The model starts with a stem, a set of plain convolutional layers without skip connections before the residual blocks. The stem comprises a 3×3 stride 2 convolution with 16 channels, two 3×3 stride 1 convolutions with 32 and 64 channels and a 3×3 stride 2 convolution with 128 channels. After the stem, the numbers of blocks for four "residual" stages are 1, 2, 6 and 3, respectively. In order to train deep ResNets without normalization, NFNet uses two scalers (α and β, see Figure 2.5) to suppress the scale of the activations. The residual stages begin with a transition block, followed by standard non-transition blocks. The difference between transition and non-transition blocks is that transition blocks downsample with a 2×2 average pooling layer on the skip path and change the output channel count via a 1×1 shortcut convolutional layer. After these residual blocks, a 1×1 expansion convolutional layer is applied to double the channel count; then, global average pooling is adopted. The final layer is a fully connected classifier layer. The original fully connected layer outputs a 1000-way class vector. The work presented in this thesis replaces the final layer with a layer that outputs a three-way class vector to match the sea ice types. At last, the fully connected layer outputs are softmaxed in order to obtain normalized class probabilities. All convolutions employ scaled weight standardization, whereas the squeeze-and-excitation layers and fully connected layers do not adopt it. The configuration of each layer is specified in Table 2.3.

Table 2.3: The configuration of the NFNet-F0 layers.

Stage	NFNet-F0	Number of Blocks
Stem	conv, 3×3, 16 conv, 3×3, 32 conv, 3×3, 64 conv, 3×3, 128	×1
Residual Blocks 1	conv, 1×1, 128 conv, 3×3, 128 conv, 3×3, 128 conv, 1×1, 256 SE	×1
Residual Blocks 2	conv, 1×1, 256 conv, 3×3, 256 conv, 3×3, 256 conv, 1×1, 512 SE	×2
Residual Blocks 3	conv, 1×1, 768 conv, 3×3, 768 conv, 3×3, 768 conv, 1×1, 1536 SE	×6
Residual Blocks 4	conv, 1×1, 768 conv, 3×3, 768 conv, 3×3, 768 conv, 1×1, 1536 SE	×3
Fully Connected	Average pool, fully connected, softmax	

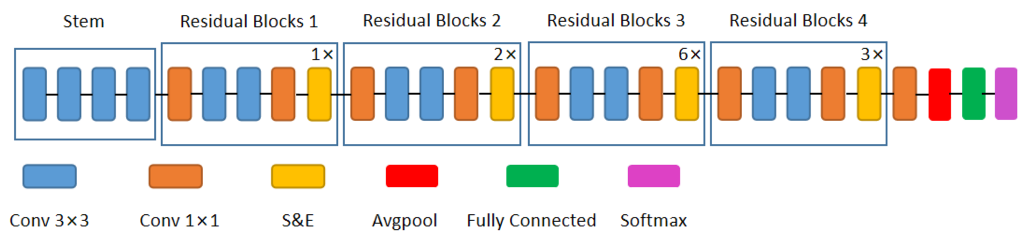

Figure 2.4: Schematic diagram of the NFNet-F0 model (compressed view).

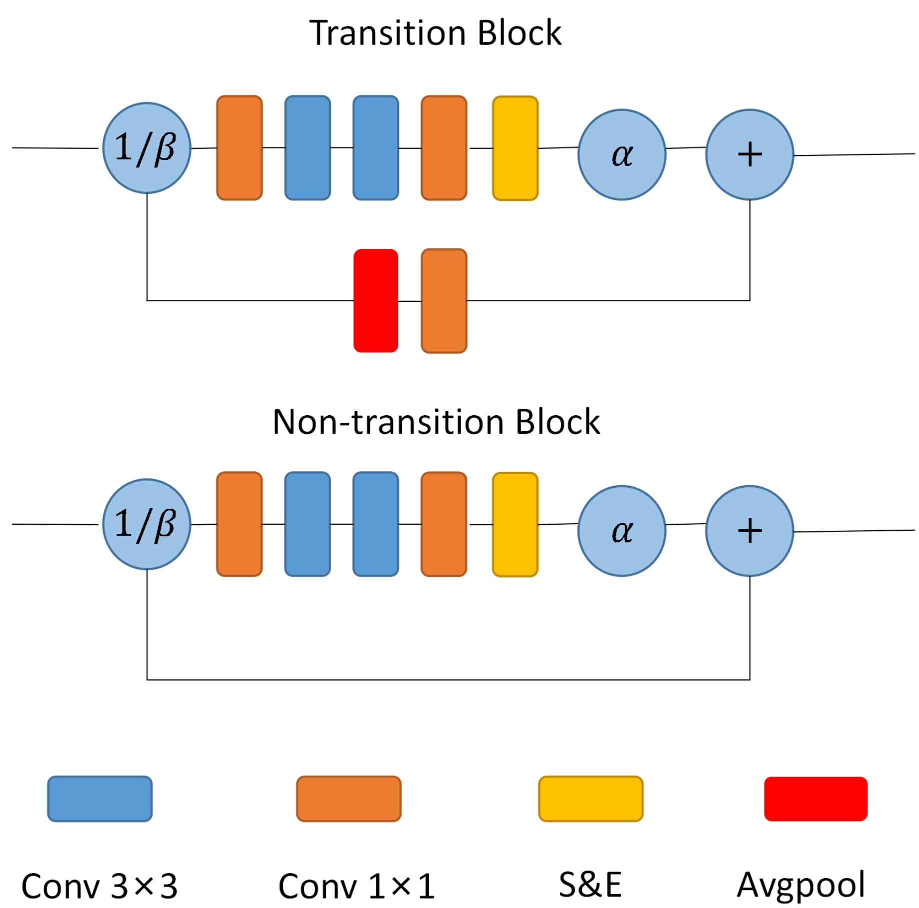

Figure 2.5: NFNet residual blocks (transition and non-transition).

2.2.2.2 Adaptive Gradient Clipping

Batch normalization (BN) is widely used in deep learning to rearrange the data distribution, making the activation function more sensitive to training data. However, BN also has some disadvantages. First, it is an expensive computational operation, which incurs memory overhead and increases the time of gradient evaluation [75]. Second, it introduces inconsistencies between the behaviors of the model during training and at inference time due to the change in the data distribution, resulting in additional hidden hyper-parameters that have to be tuned [75]. Third, it is difficult to replicate batch-normalized networks precisely on different hardware. Different hardware may be used to train different batches of data at the same stage since some GPUs with low RAM cannot be used to train a model with a very high batch size [75].

Adaptive gradient clipping (AGC) is applied in the NFNet to train ResNets without batch normalization. In the AGC algorithm, the i-th row of the gradient of the l-th layer G_i^l is clipped as [75]:

$$G_i^l = \begin{cases} \lambda \frac{\|W_i^l\|_F^*}{\|G_i^l\|_F} G_i^l & if \frac{\|G_i^l\|_F}{\|W_i^l\|_F^*} > \lambda, \\ G_i^l & otherwise. \end{cases} \quad (2.3)$$

where λ is the clipping threshold, and $\| W_i^l \|_F^* = \max(\| W_i^l \|_F, \epsilon)$, with default $\epsilon = 10^{-3}$; $\| \cdot \|_F$ denotes the Frobenius norm.

2.2.2.3 Preprocessing of the Inputs

HH, HV and the cross-polarization ratio were extracted from the RCM images as inputs. In this study, the cross-polarization ratio was defined as $\sigma_{HV}^0/\sigma_{HH}^0$ and was used as an input channel for the NFNet classification, since it was found to be able to improve the discrimination between open water and ice types [43]. The patch size was set to 7 × 7 to compare with the RF method (the window size of GLCM features for RF is 7 × 7). Since the inputs fed into the NFNet are supposed to be fixed in size, all the sampled sub-regions were first resized using bilinear interpolation. In this study, NFNet-F0 was adopted here and its input size for training was 192 $\times$ 192 $\times$ 3, and 256 $\times$ 256 $\times$ 3 for testing. Then, the resized inputs were normalized using mean = [0.485, 0.456, 0.406], and std = [0.229, 0.224, 0.225] for three input channels, respectively [75].

2.2.2.4 Training Strategy

The training strategy of the NFNet-F0 was basically the same as that in [75]. Softmax cross-entropy loss was used with label smoothing of 0.1. Stochastic gradient descent was applied with Nesterov's momentum coefficient of 0.9 and a weight decay coefficient of 0.00002. The learning rate warmed up from 0 to its maximal value of 0.05 over the first five epochs (iterations). After the warmup, the learning rate was cosine-annealed to zero. AGC was set with $\lambda = 0.01$ for every parameter except the fully connected layer. An exponential moving average was implemented with a decay rate of 0.99999 and followed a warmup schedule where the decay was equal to $\min(0.99999, 1 + t/10 + t)$, where t was the number of iterations. The batch size was set as 128. For the training process, 70% of samples were used to train the model, and 30% of samples were used to evaluate the model's generalization ability. Three hundred and sixty epochs were executed to train the model. Figure 2.6 shows the validation accuracy changes with epochs during the training process. After about 130 epochs, the validation accuracy of the model tended to be stable. The model with the best validation accuracy was obtained for subsequent classifications.

2.2.3 Random Forest

RF is an ensemble machine-learning technique that creates a group of decision trees (DTs) as weak learners [91]. The majority of votes decide the classification result from these decision trees. DTs are trained by means of a bagging strategy that generates multiple bootstrapped data sets from the original training data. Because of the use of bagging and ensemble strategies, the RF classifier is characterized by low variance and low bias, which

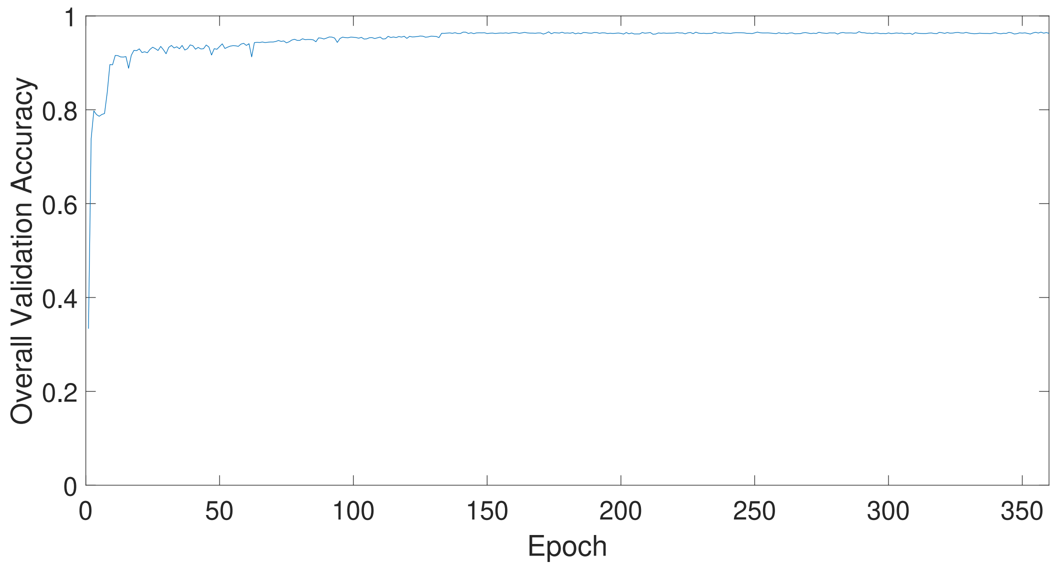

Figure 2.6: Epochs versus validation accuracy.

means it is robust and less sensitive to the quality of the training data [91]. Various machine learning algorithms have been applied for sea ice sensing in the past decade, such as the support vector machine (SVM) [92], random forest (RF) [64], convolutional neural network (CNN) [93], and long short-term memory (LSTM) [32] methods. In [94], a meta-analysis of 251 peer-reviewed journal papers was performed to compare RF with SVM for remote sensing image classification. According to the meta-analysis database, the authors concluded that RF outperforms SVM in most cases. In this study, RF was adopted as a top-ranked conventional machine learning algorithm to compare with NFNet. In the future, NFNet will be compared to other state-of-the-art neural networks. Two levels of RF classification were applied in this study. Ice and water were classified for the 1st level, then the identified ice pixels were classified as NI or OI/FYI at the 2nd level.

HH, HV, the cross-polarization ratio and the gray-level co-occurrence matrix (GLCM) features of the RCM dual-polarized GRD images were used for sea ice detection and classification. GLCM represents the frequency that a pixel pair in a specific direction appears in a grayscale image. First, the grayscale image was normalized to n levels. Then, the number of times every possible pair (for example, 0,1) appeared in a particular direction was counted and filled into the corresponding matrix for this direction. For example, m_{ij}

in a horizontal GLCM indicates that the pair (i, j) in the horizontal direction appears m times, and m is located at the ith row and jth column in the matrix. After that, the mean, variance, correlation, homogeneity, contrast, dissimilarity, entropy, angular second moment and maximum probability can be calculated according to the GLCM matrix. These features can be used as texture features for further analysis. According to [95], 64 levels and 4 (0°, 45°, 90°, 135°) orientations were the recommended GLCM parameters for sea ice detection in SAR images. For this study, a displacement of 1 and window of size 7×7 were selected. Such a window size was selected in order to be consistent with the speckle-filtering window. The authors of [96] investigated the nine GLCM features and found that mean and variance were effective for both HH and HV channels. In this study, a mean displacement and mean orientation (MDMO) strategy for GLCM was applied. In other words, the average values of the GLCM mean and variance in four orientations of one channel were extracted separately. Finally, four features (the GLCM mean of HH, GLCM variance of HH, GLCM mean of HV and GLCM variance of HV) were obtained.

Ten-thousand samples from March 1 were labeled for each class. The number of trees, maximum tree depth, maximum features, minimum samples-split and minimum samples-leaf were tuned based on five-fold cross-validation. After cross-validation, the parameters for the two-level RF model were set as shown in Table 2.4.

Table 2.4: Two-level RF classification parameters.

Parameters	**1st-level RF**	**2nd-level RF**
Number of trees	500	500
Maximum tree depth	15	8
Maximum features	6	5
Minimum samples-split	50	50
Minimum samples-leaf	10	10

2.3 Experiment Result and Discussion

Figures 2.7–2.9 illustrate the analysis results for March 1, March 2 and January 4, respectively. The green rectangles in Figure 2.7 (a) were used for selecting the training samples

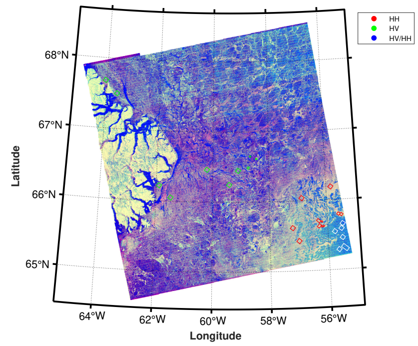

(**a**) Pseudo color image.

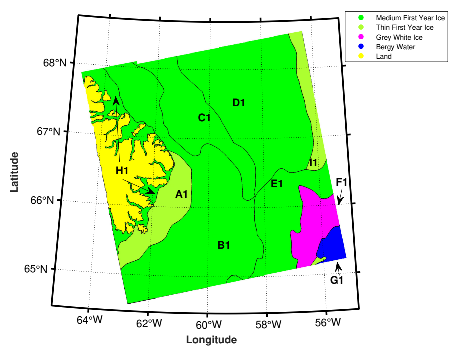

(**b**) Sea ice chart.

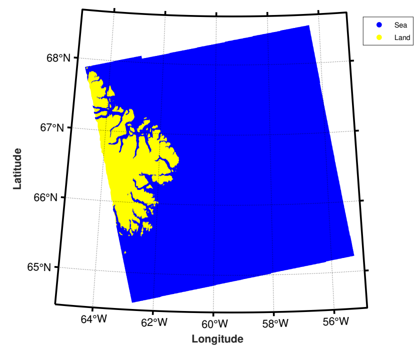

(**c**) Land mask.

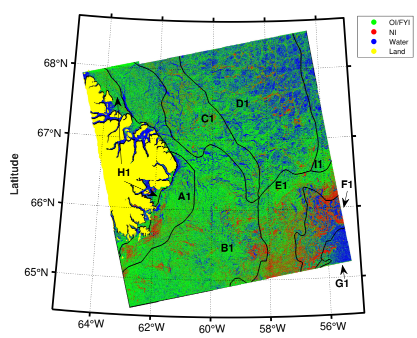

(**d**) RF classification result.

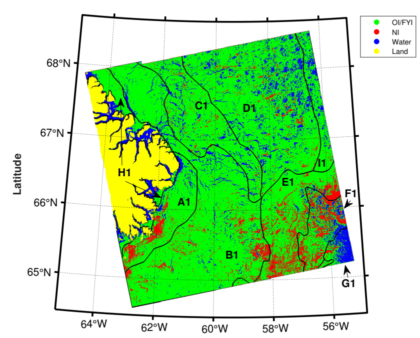

(**e**) NFNet classification result.

Figure 2.7: (**a**) Image acquired on March 1 2021. The green rectangles display the locations of the training samples for OI/FYI. The red and white rectangles indicate the areas of the training and testing samples for NI and water, respectively. (**b**) Sea ice chart. (**c**) Land mask. (**d**) RF classification result. (**e**) NFNet classification result.

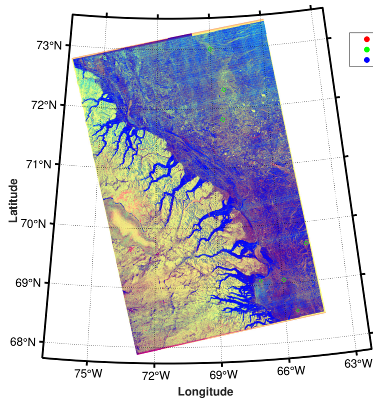

(**a**) Pseudo color image.

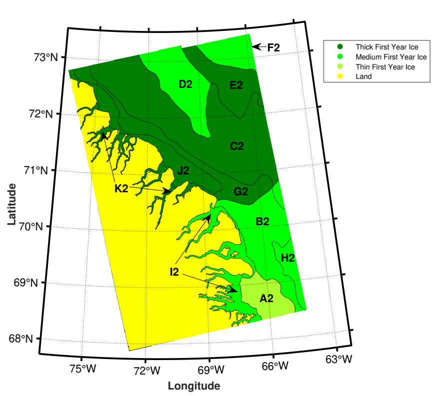

(**b**) Sea ice chart.

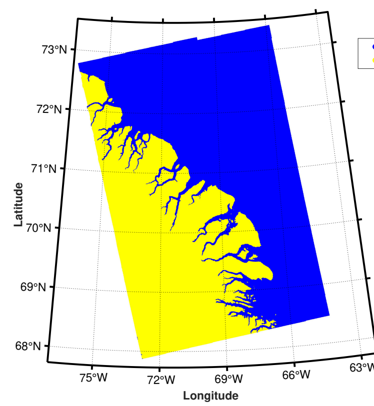

(**c**) Land mask.

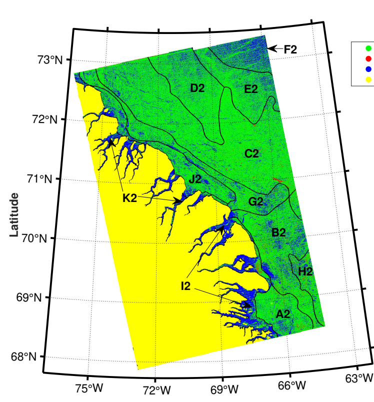

(**d**) RF classification result.

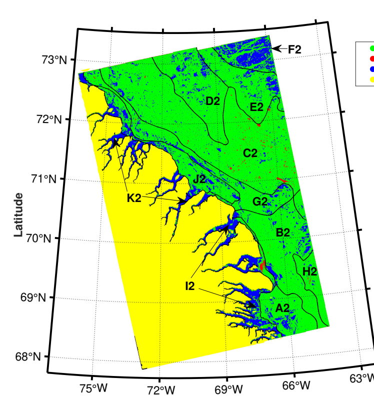

(**e**) NFNet classification result.

Figure 2.8: (**a**) Image acquired on March 2 2021. The green rectangles display the locations of the testing samples for OI/FYI. (**b**) Sea ice chart. (**c**) Land mask. (**d**) RF classification result. (**e**) NFNet classification result.

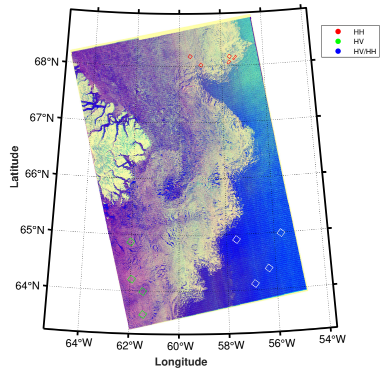

(**a**) Pseudo color image.

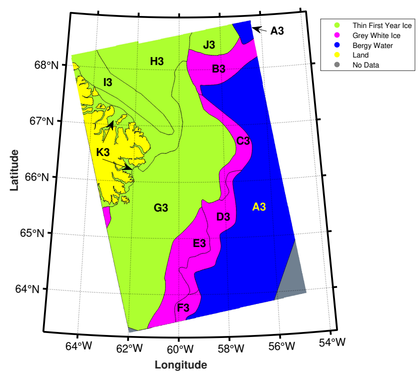

(**b**) Sea ice chart.

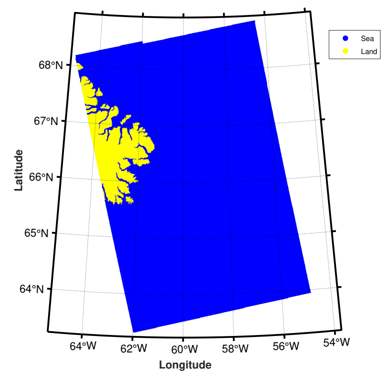

(**c**) Land mask.

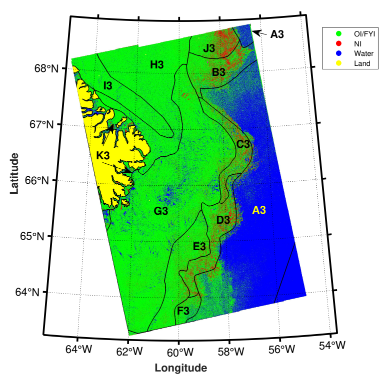

(**d**) RF classification result.

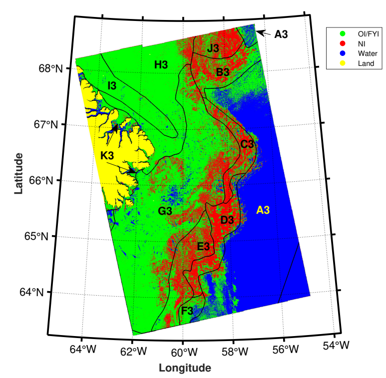

(**e**) NFNet classification result.

Figure 2.9: (**a**) Image acquired on January 4 2021. The green, red and white rectangles indicate the areas of the testing samples of OI/FYI, NI and water, respectively. The testing samples were at least 100 kilometers away from the March 1st training samples. (**b**) Sea ice chart. The area without sea ice chart data is indicated in gray. (**c**) Land mask. (**d**) RF classification result. (**e**) NFNet classification result.

for OI/FYI. The red and white rectangles indicate the areas used for selecting the training and testing samples of NI and water, respectively, and their testing samples were located far away from corresponding training samples, as mentioned in Section 2.1.4.

The green rectangles presented in Figure 2.8 (a) were used for extracting the OI/FYI samples for the first testing set. Ten-thousand samples for each class of the second testing set were obtained from the rectangles displayed in Figure 2.9 (a). Compared to the training samples, the corresponding second testing samples were taken from a different time (January 4) and different regions. All the testing samples for the two techniques were the same. The RF method's overall accuracy, F1 score, and the kappa coefficient of the first testing set were 87.42%, 0.8791, and 0.8113, respectively. For the NFNet classification, the first testing set's overall accuracy was 99.78%, the F1 score was 0.9978 and the corresponding kappa coefficient was 0.9967. As for the second testing set, the RF's overall accuracy, F1 score, and kappa coefficient were 78.73%, 0.8153, and 0.6895, whereas NFNet's overall accuracy, F1 score, and kappa coefficient were 98.18%, 0.9821, and 0.9727. Although different data sets and cover types were used, the overall accuracies of RF (87.42% and 78.73%) and NFNet (99.78% and 98.18%) in this study were close to that of RF (87%) in [64] and VGG-16 (99.89%) in [72]. It should be noted that although the accuracy of VGG-16 for the data set created in [72] is very high, some water regions of the SAR images were misclassified into ice by the VGG-16 model. Those regions were displayed as long stripes due to the interference of the thermal noise in the HV channel. The corresponding confusion matrices are displayed in Figure 2.10. For the first testing set (see Figures 2.10 (a) and (b)), no ice samples were misclassified by the NFNet as water. For the RF model, the classification accuracy for water was only 87.96%, which means that more ice samples were misclassified as water. Moreover, the recall of OI/FYI was 73.09%. For the two-level RF model, OI/FYI was classified at the second level, distinguishing OI/FYI and NI from ice samples. The poor recall for OI/FYI indicates that many OI/FYI samples were misclassified as NI. Figures 2.10 (c) and (d) illustrate the confusion matrices of the two models for the second testing set. It can be seen that the accuracy of the NFNet for NI only dropped slightly. The 100% accuracy for water displayed by the NFNet may be because these water samples were very far from the main ice area. Only 41.35% of the NI samples from the second testing were correctly classified for the RF method, and more than half of the NI samples were misclassified as OI/FYI.

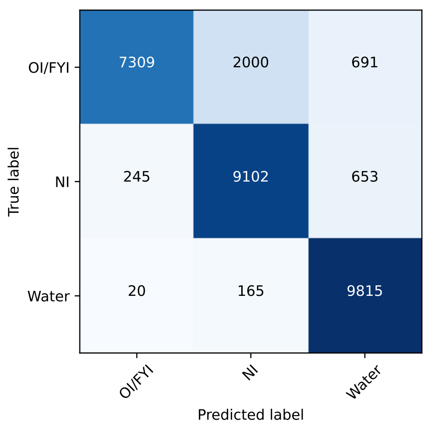

(**a**) RF (March 1 and 2).

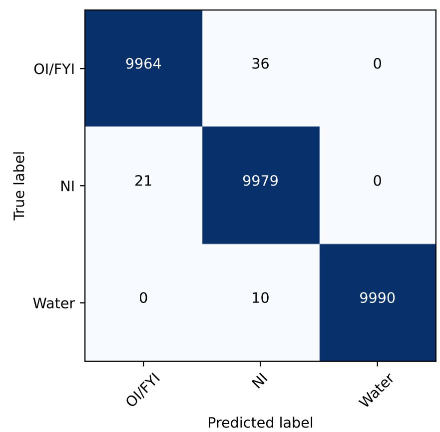

(**b**) NFNet (March 1 and 2).

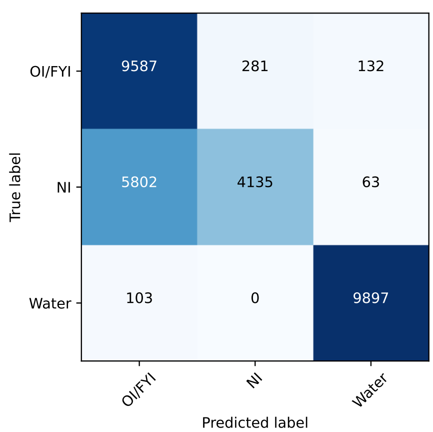

(**c**) RF (January 4).

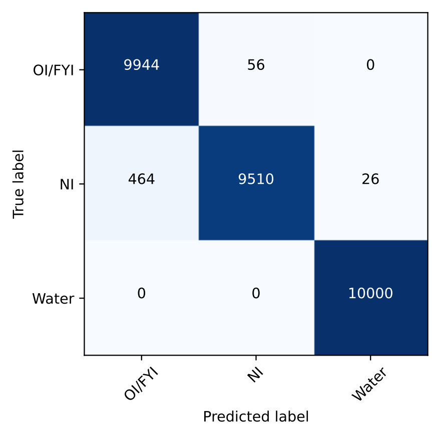

(**d**) NFNet (January 4).

Figure 2.10: Confusion matrices of the RF and NFNet models.

Figure 2.11 illustrates the t-SNE images of the second last layer of the NFNet, which illustrates the ability of the model to distinguish between sea ice and water. Thirty-thousand testing samples were applied as inputs to display each t-SNE diagram. The features from the NFNet were perfectly clustered. However, the feature clusters of OI/FYI and NI showed some degree of confusion.

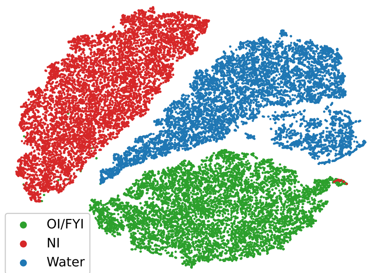

(**a**)

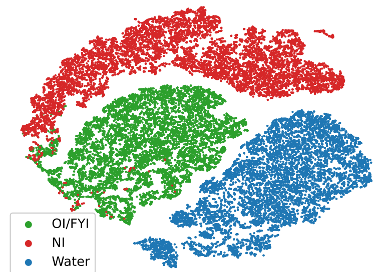

(**b**)

Figure 2.11: 2-D feature visualizations of the sea ice classes from the two testing sets, using the t-SNE algorithm for the second last layer of the NFNet. (**a**) The t-SNE diagram of the first testing set. (**b**) The t-SNE diagram of the second testing set.

Tables 2.5–2.7 show comparisons of the sea ice chart data, the RF and NFNet results. In these tables, the "area ratio" represents the ratio of the area of a polygon (which may be incomplete) in an RCM image to that of the corresponding complete polygon in the sea ice chart. A higher "area ratio" for a polygon means that the data for this area shown in the RCM image are more representative than those of the complete polygon.

Figure 2.7 demonstrates the classification results of the full image from March 1. As mentioned earlier, the training samples for the two-level RF classification model and the NFNet model were selected from this image. Figures 2.7 (d) and (e) depict the RF and NFNet classification results. Although only samples from region G1 were labeled as water, both classification results show that all the dark blue regions in the pseudo-color images were identified as water. In general, more regions were classified as water by RF than NFNet. Both classifiers detected NI at approximately the same locations. Although more pixels were classified as NI by the RF model, except in region F1, for which the NI concentrations estimated using the two models were very close, with a difference of only 0.5% (see Table 2.5). In the digital sea ice chart, no NI was reported in regions B1, C1, D1, G1, H1 or I1. However, both methods detected less than 10% NI in these regions. According to the notation principles of sea ice chart [1], any ice type with a concentration less than 10% would not be reported; therefore, the NI estimation results of these regions are reasonable.

Table 2.5: Comparison of the estimated concentration for March 1.

Region	**Area Ratio**	**Results**	**OI/FYI**			**NI**		**Total Concentration**
			OI	**MFYI**	**TFYI**	**GWI**	**GI**	
A1	90.2%	Chart	0	0	60%	**30%**	**10%**	90%+
		RF	67.2%			**16%**		83.2%
		NFNet	77.2%			**15.5%**		92.7%
B1	50.2%	Chart	0	90%	0	0	0	90%+
		RF	69.9%			9.7%		79.6%
		NFNet	88.7%			6.1%		94.8%
C1	25.1%	Chart	20%	80%	0	0	0	90%+
		RF	63.2%			9.8%		73%
		NFNet	86.5%			4%		90.5%
D1	26.4%	Chart	0	90%+	0	0	0	90%+
		RF	54.1%			6.9%		**61%**
		NFNet	81.7%			3.6%		85.3%
E1	41%	Chart	0	60%	40%	0	0	90%+
		RF	60.4%			26.8%		87.2%
		NFNet	72.6%			25.2%		97.8%
F1	49%	Chart	0	0	20%	30%	30%	90%
		RF	38.1%			**32.2%**		70.3%
		NFNet	51.8%			**33.7%**		85.5%
G1	0.1%	Chart	0	0	0	0	0	<10%
		RF	29%			7.3%		**36.3%**
		NFNet	33.6%			6.8%		**40.4%**
H1	35.3%	Chart	0	100%	0	0	0	100%
		RF	47.3%			6.2%		**53.5%**
		NFNet	52.4%			3.3%		**55.7%**
I1	10%	Chart	0	30%	70%	0	0	90%+
		RF	54.1%			5.1%		**59.2%**
		NFNet	79.1%			1.8%		80.9%

Table 2.6: Comparison of the estimated concentration for March 2.

Region	**Area Ratio**	**Results**	**OI/FYI**				**NI**	**Total Concentration**
			OI	**TKFYI**	**MFYI**	**TFYI**		
A2	79%	Chart	0	0	30%	70%	0	90%+
		RF	83.1%				3.1%	86.2%
		NFNet	87.3%				0.3%	87.6%
B2	19.3%	Chart	0	0	90%+	0	0	90%+
		RF	72.9%				4.8%	77.7%
		NFNet	90.5%				0.2%	90.7%
C2	77.2%	Chart	20%	40%	40%	0	0	90%+
		RF	84.8%				2.2%	87%
		NFNet	94.7%				1.5%	96.2%
D2	29%	Chart	0	0	90%+	0	0	90%+
		RF	81.1%				0.6%	81.7%
		NFNet	89.2%				0.2%	89.4%
E2	46.6%	Chart	0	50%	50%	0	0	90%+
		RF	77.1%				0.4%	77.5%
		NFNet	87.2%				0.3%	87.5%
F2	4.4%	Chart	0	30%	70%	0	0	90%+
		RF	52.3%				0.2%	**52.5%**
		NFNet	46%				0.5%	**46.5%**
G2	88.6%	Chart	0	50%	50%	0	0	90%+
		RF	75.8%				2.4%	78.2%
		NFNet	87.2%				0.4%	87.6%
H2	7.1%	Chart	20%	0	80%	0	0	90%+
		RF	74.5%				6.3%	80.8%
		NFNet	95%				1.2%	96.2%
I2	42.9%	Chart	0	0	100%	0	0	100%
		RF	30.5%				2.1%	**32.6%**
		NFNet	40.4%				3.2%	**43.6%**
J2	99.6%	Chart	0	100%	0	0	0	100%
		RF	70.9%				0.9%	71.8%
		NFNet	74.8%				<0.1%	74.8%
K2	11.7%	Chart	0	100%	0%	0	0	100%
		RF	26.5%				0.7%	**27.2%**
		NFNet	36.9%				2.3%	**39.2%**

Table 2.7: Comparison of the estimated concentration for 4 January.

Region	**Area Ratio**	**Results**	**OI/FYI**	**NI**			**Total Concentration**
			TFYI	**GWI**	**GI**	**NI**	
A3	30.8%	Chart	0	0	0	0	<10%
		RF	21.6%	1.7%			**23.3%**
		NFNet	16%	2.6%			**18.6%**
B3	86.5%	Chart	0	30%	30%	20%	80%
		RF	68.3%	**19.2%**			87.5%
		NFNet	50.8%	**46.2%**			97%
C3	66.2%	Chart	70%	30%	0	0	90%+
		RF	69.5%	24%			93.5%
		NFNet	33%	**63.6%**			96.6%
D3	100%	Chart	0	50%	20%	20%	90%
		RF	69.3%	**24.6%**			93.9%
		NFNet	27.5%	**66.9%**			94.4%
E3	87.8%	Chart	20%	70%	10%	0	90%+
		RF	87.4%	**9.2%**			96.6%
		NFNet	45.8%	**53.5%**			99.3%
F3	67.5%	Chart	0	30%	10%	10%	50%
		RF	82.3%	**8.3%**			**90.6%**
		NFNet	69.5%	**15.3%**			**84.8%**
G3	92.3%	Chart	70%	30%	0	0	90%+
		RF	89%	**3%**			92%
		NFNet	78.6%	**17.5%**			96.1%
H3	27%	Chart	90%+	0	0	0	90%+
		RF	93%	0.9%			93.9%
		NFNet	93.8%	5.2%			99%
I3	66.2%	Chart	90%+	0	0	0	90%+
		RF	93.9%	0.6%			94.5%
		NFNet	97.9%	1%			98.9%
J3	22.4%	Chart	80%	20%	0	0	90%+
		RF	66.2%	31.4%			97.6%
		NFNet	30.3%	**69.5%**			99.8%
K3	40.1%	Chart	100%	0	0	0	100%
		RF	75.9%	6.1%			**82%**
		NFNet	65.4%	7.3%			**72.7%**

Meanwhile, the NI concentrations of regions A1, E1 and F1 derived using the two models were higher than 10%, but the sea ice chart reports very high NI concentrations in regions A1 (40%) and F1 (60%) and no NI in region E1. Because the training samples of NI were only selected from the subarea with a uniform ice distribution in region F1, but NI includes many types (rind, nilas, gray ice, gray-white ice) and forms (pancake, ice cake, ice floe) that may show different scattering characteristics [1], the training data may not represent all the types of NI in the regions, which leads to the estimation difference in these areas. Although the sea ice chart reports no NI in E1, both RF and NFNet detected NI at similar locations, and their concentration values were also very close. The area ratio of E1 was only 41%, indicated that perhaps there was very little NI in the portion that belonged to the same polygon E1 but was not covered by the RCM image. Moreover, considering that E1 is adjacent to F1, it is reasonable that NI exists in E1. Thus, the results of NFNet and RF may be more reliable than the weekly sea ice chart for region E1. Field exploration data are required for further validation. As for the total concentration, the results of NFNet and RF were in agreement with the sea ice chart data for most of the regions, with the former showing a better agreement. In particular, the RF-estimated total ice concentrations of D1 and I1 were 61% and 59.2%, respectively, which were not consistent with the sea ice chart (90%+ for both regions, see Table 2.5). On the contrary, NFNet's results were 85.3% and 80.9% for these two regions. Considering that no training data came from D1 and I1, this difference proves that the generalization ability of NFNet was better than that of RF. In addition, the sea ice concentrations of G1 estimated by both classifiers were higher than 10%, although the sea ice chart displays a concentration less than 10%. However, the area ratio of G1 was only 0.1%, which means that only the edge of the polygon G1 was covered by the RCM image from March 1 and the value is very unrepresentative. Therefore, the deviation of the two classifiers in G1 is understandable. It can also be observed that the classification results for the regions near the coast are similar for both classifiers. Based on the above analysis, it can be inferred that the NFNet method can produce more reasonable sea ice estimation results than the RF method.

The classification results from the image acquired on March 2 are displayed in Figures 2.8 (d) and (e). It should be highlighted that no samples from the March 2 image were used for training the classification models. Similarly to the March 1 image results, both models provided good classification results in general, and more water regions were identified by the RF model than the NFNet. The NI percentages in both results were also very low, which was in agreement with the digital sea ice chart. The total sea ice concentration estimation results of the NFNet obtained from A2, B2, C2, D2, E2 and G2 were consistent with that of the sea ice chart, except for F2 (see Table 2.6). Considering that F2 had the lowest area ratio (4.4%) in the March 2 image, only part of this polygon was analyzed and the results may not represent the sea ice condition of the majority of the polygon, so this deviation is reasonable. It can be seen in Figures 2.7 and 2.8 that H1, I2, J2 and K2 are next to the coast. The sea ice chart reported that those regions were occupied by fast ice, which was "fastened" to the coastline and can extend from a few meters or several hundred kilometers from the coast [1]. For fast ice regions, there were some gaps between the estimation results and the sea ice chart data. Although J2's area ratio was close to 100% and the corresponding sea ice chart data indicated that this area was covered by consolidated ice (100% concentration), the pseudo-color image Figure 2.8 (a) exhibits many dark blue strips (i.e., water) in this area. Therefore, at least on March 2, the sea ice concentration in J2 should not be 100%. Furthermore, the time resolution of the sea ice chart adopted here was one week; therefore, the estimations of NFNet and RF are more reasonable.

In order to demonstrate the robustness of the method in terms of location and time, another image (see Figure 2.9 (a)) that was collected from different areas and times (January 4) was used. The classification results from this image are displayed in Figures 2.9 (d) and (e). Both models provided good classification results for OI/FYI and water. However, the RF model identified fewer NI regions than the NFNet. The NI percentages in both results were lower than those of the sea ice chart (see results of B3, D3, E3, F3 and G3, which are highlighted in bold in Table 2.7), but the NI concentrations estimated by NFNet were closer to those of the sea ice chart. In other words, NFNet provides better generalization ability for NI than the RF method. For C3 and J3, the NI concentration obtained by RF was close to the corresponding reports of the sea ice chart, whereas the NI concentration determined by RF was much higher. Considering the relatively poor performance of the RF classifier for these regions and the fact that the pseudo-color image (Figure 2.9 (a)) also shows that C3 and J3 regions are uniformly bright white (i.e., covered by new ice), the NI classification by NFNet should be more reliable. The total concentration differences of A3 and K3 are also due to the presence of landfast ice and glacier ice, as discussed above. For F3, the total concentrations estimated by the two classifiers were both significantly higher than the sea ice chart results. The pseudo-color image (Figure 2.9 (a)) shows that only a tiny proportion of F3 is blue (i.e., covered by water), so the total concentration of F3 should be higher than 50%, at least for January 4.

According to the experimental results, the high accuracy and kappa coefficient show the superior performance of the NFNet model over the RF model. Confusion matrices indicate that the RF model underestimated the total concentration and significantly underestimated the NI concentration due to the time difference. The challenge of classifying the new ice types is also demonstrated in previous works [9, 55, 64]. However, the NFNet model showed more generalization ability for classifying NI than the RF model. Although our training dataset was unbalanced and limited, considering the classification performance of the deep CNN after obtaining enough diverse data, the NFNet also shows the potential to classify NI more accurately than conventional machine learning techniques. The t-SNE diagram generated using the second testing set shows that more samples of NI were interlaced with the OI/FYI samples, which means that the NI classification accuracy of the NFNet may differ slightly due to the difference in the time and location of the samples. For the classification results of the whole images, both models showed an appropriate ability to distinguish between water and ice. By comparing the sea ice concentrations calculated based on the classification results with the concentrations obtained from sea ice charts, the NFNet results were not only better than those of RF but were also more accurate than the sea ice charts.

2.4 Classification Results in the Davis Strait, 2021

Figures 2.12 - 2.23 illustrate the classification results based on the NFNet classifier from the Davis Strait for the whole year of 2021. It should be noted that the publication date of the weekly regional ice charts released by the Canadian Ice Service cannot match the acquisition date of all RCM images displayed here. Therefore, the nearest available ice charts are illustrated in these figures. The white rectangles indicate the overlapping area of the 24 RCM images. The classification results are consistent with the sea ice charts. From the classification results, it can be seen that the sea ice extent increased to a maximum in early April and began to melt in late April. Sea ice almost completely disappeared in September, and it appeared and started developing again in late November. Although the classification results show the potential of the NFNet classifier to classify sea ice images throughout the year, some classification results are still affected by thermal noise during the melt season. Classification results for year-round sea ice images may be further improved by separately training classifiers for freezing and melting seasons.

2.5 Chapter Summary

This chapter presents the first case study of a sea ice classification application using actual RCM dual-polarized data with an emerging AI technique (NFNet). Destriping was considered to mitigate the thermal noise in the HV channel in addition to conventional SAR preprocessing steps. HH, HV and the cross polarization ratio were extracted from three RCM images, collected from the Eastern Arctic for the NFNet sea ice classifier. The classification results were validated using digital sea ice charts and testing samples that were different from the training samples in both space and time. A two-level RF classifier was applied as a conventional machine learning method in comparison with the NFNet method. The experimental results showed that a high accuracy of sea ice classification was achieved using dual-polarized RCM data. Good classification results proved the superiority of NFNet-based

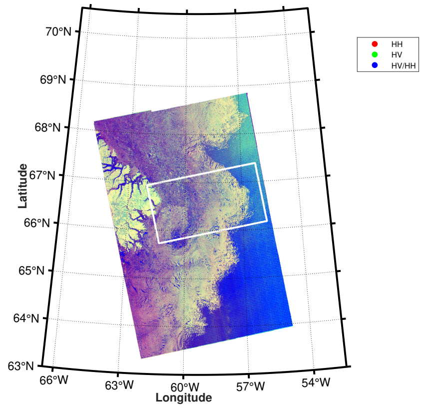

January 4 pseudo color image.

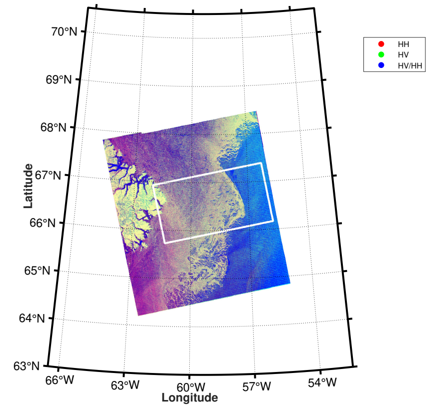

January 24 pseudo color image.

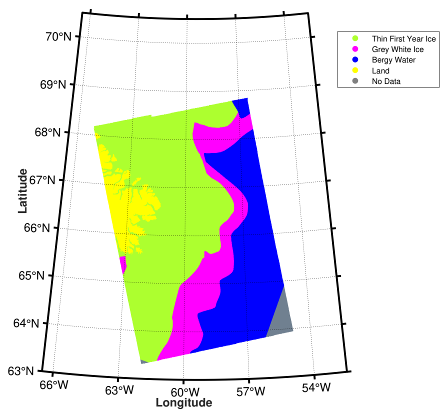

January 4 sea ice chart.

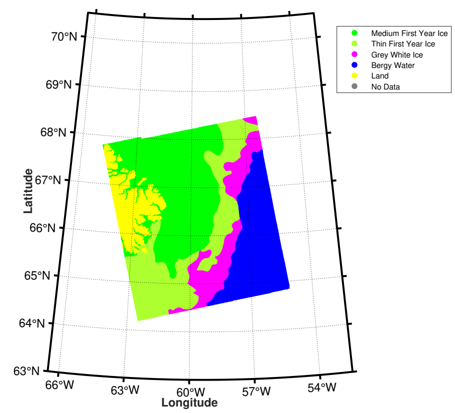

January 25 sea ice chart.

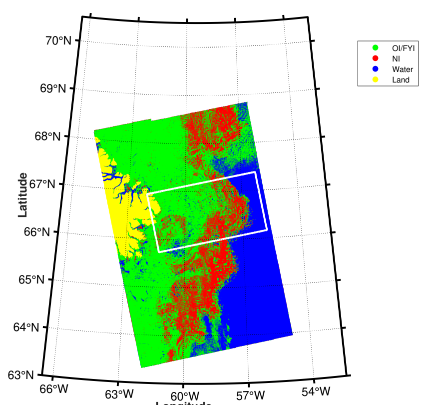

January 4 classification result.

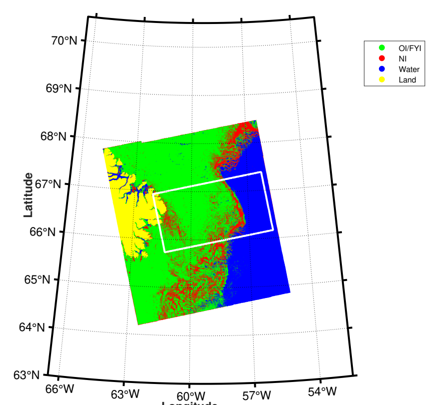

January 24 classification result.

Figure 2.12: January 4 and January 24, 2021.

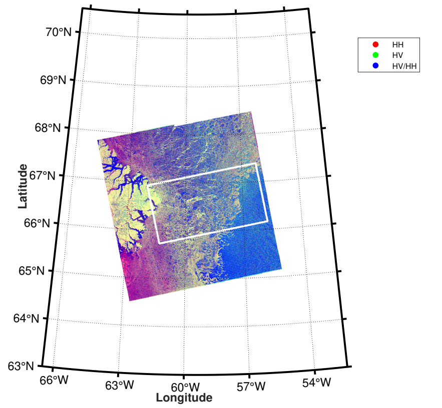

February 1 pseudo color image.

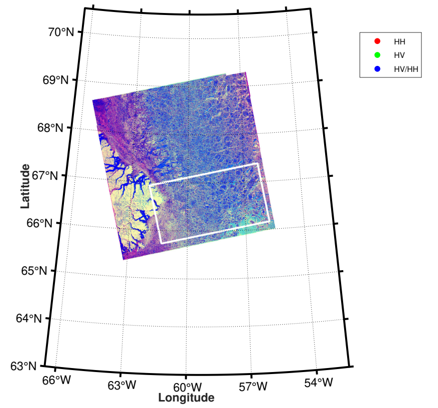

February 21 pseudo color image.

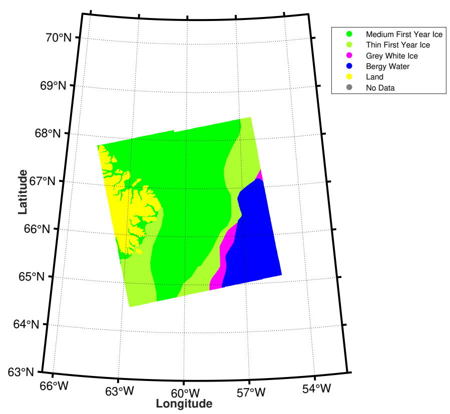

February 1 sea ice chart.

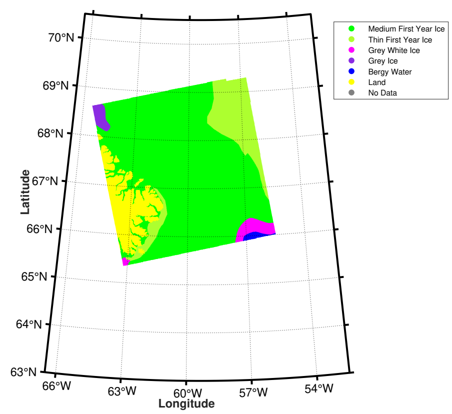

February 22 sea ice chart.

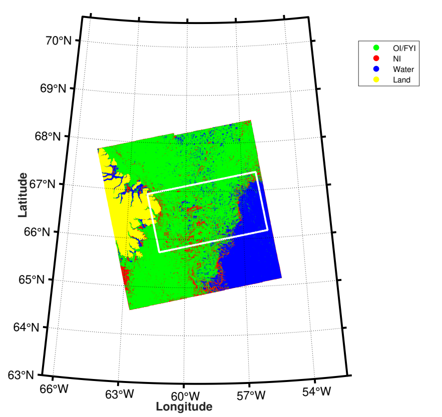

February 1 classification result.

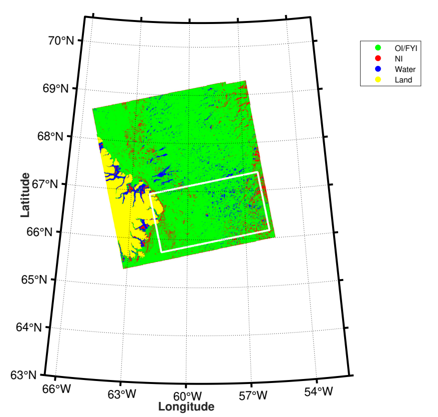

February 21 classification result.

Figure 2.13: February 1 and February 21, 2021.

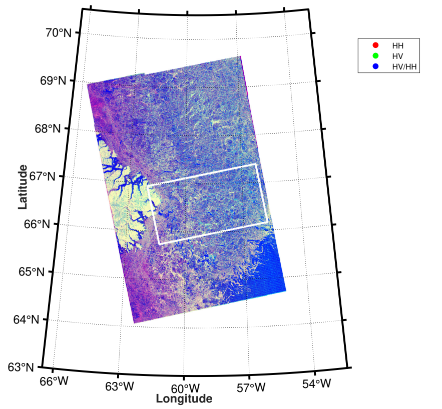

March 9 pseudo color image.

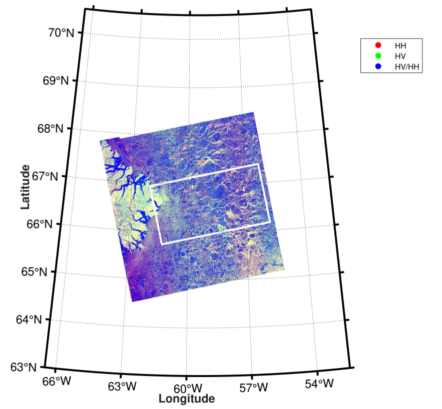

March 29 pseudo color image.

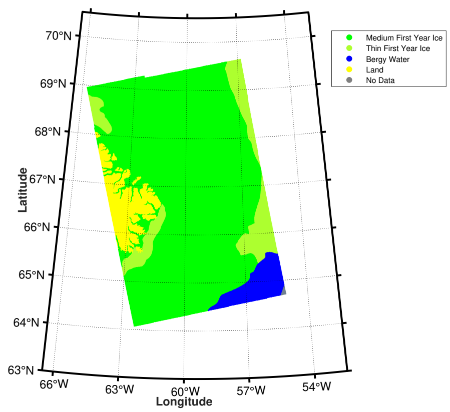

March 8 sea ice chart.

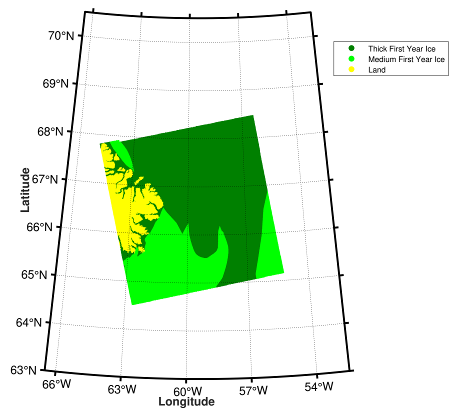

March 29 sea ice chart.

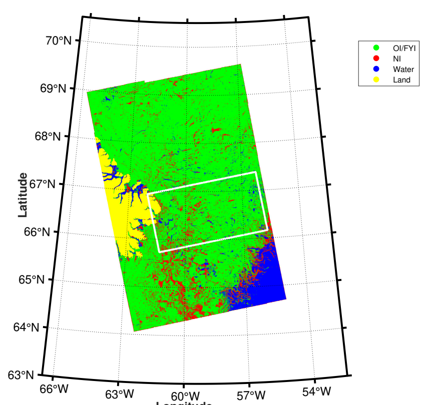

March 9 classification result.

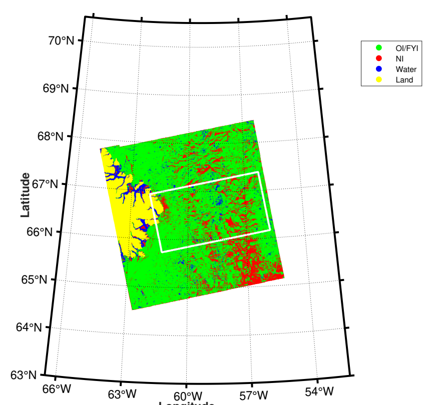

March 29 classification result.

Figure 2.14: March 9 and March 29, 2021.

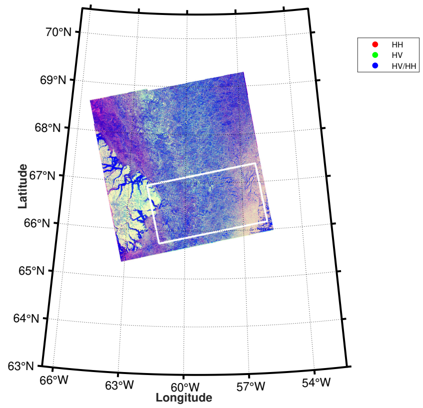

April 6 pseudo color image.

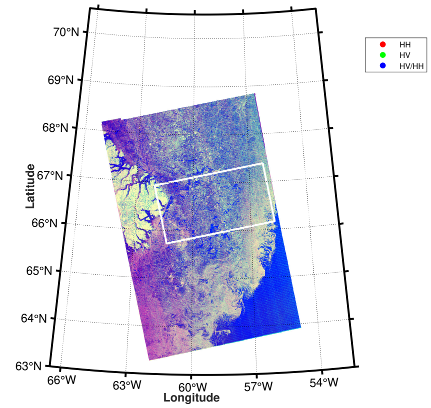

April 22 pseudo color image.

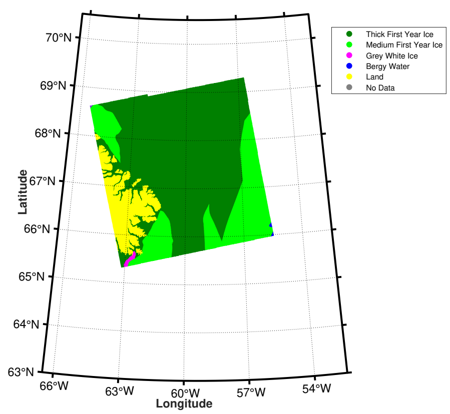

April 5 sea ice chart.

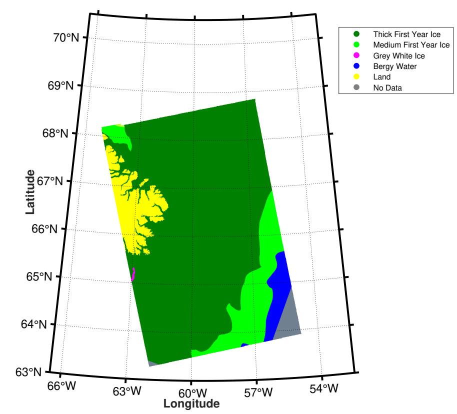

April 19 sea ice chart.

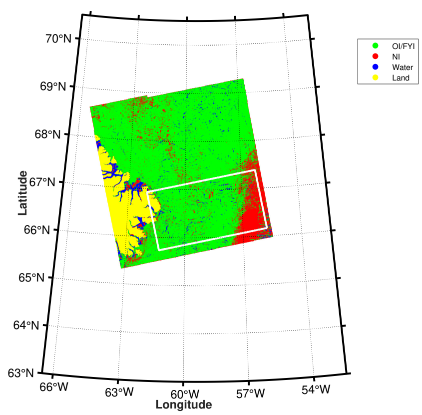

April 6 classification result.

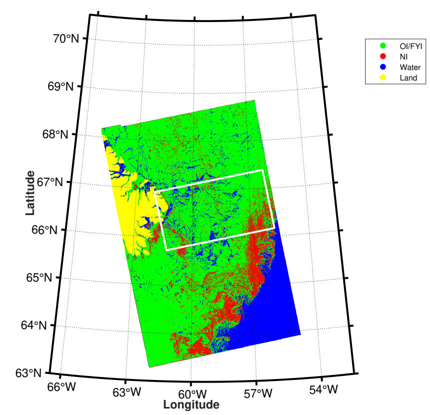

April 22 classification result.

Figure 2.15: April 6 and April 22, 2021.

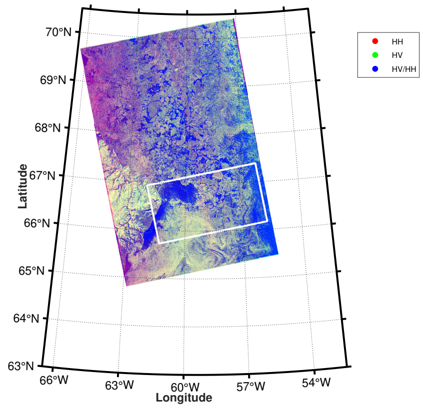

May 16 pseudo color image.

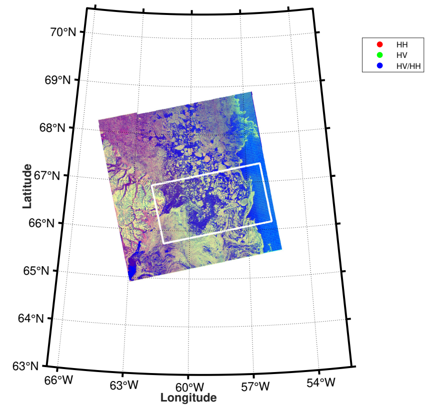

May 24 pseudo color image.

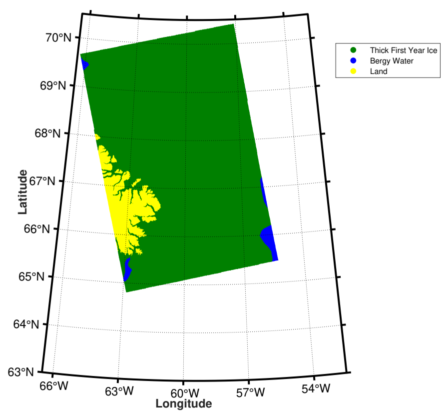

May 17 sea ice chart.

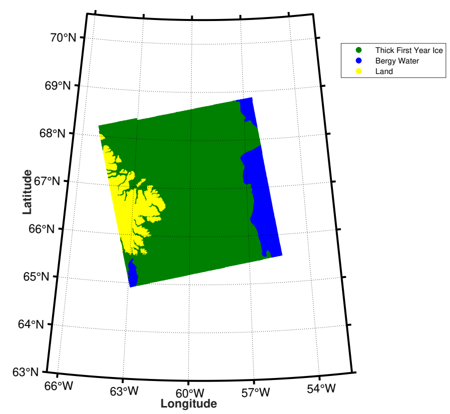

May 24 sea ice chart.

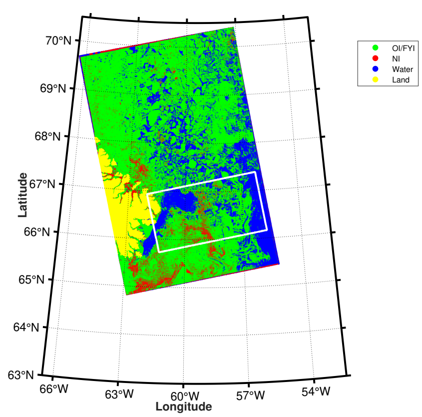

May 16 classification result.

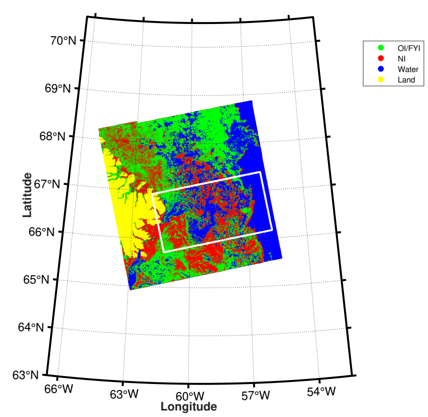

May 24 classification result.

Figure 2.16: May 16 and May 24, 2021.

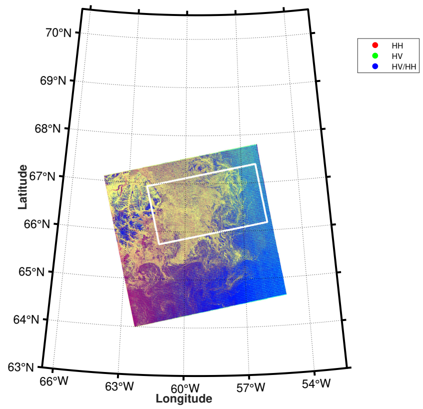

June 17 pseudo color image.

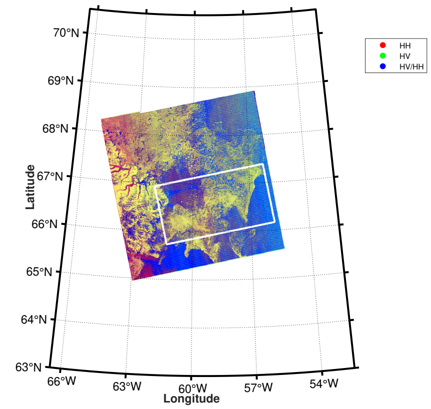

June 29 pseudo color image.

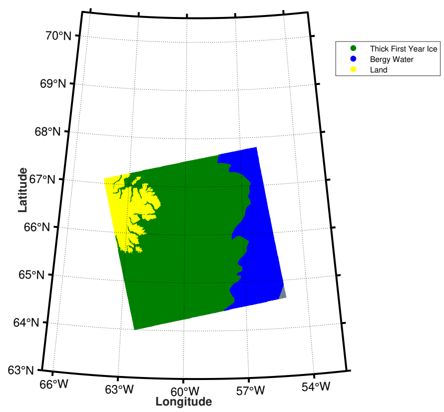

June 14 sea ice chart.

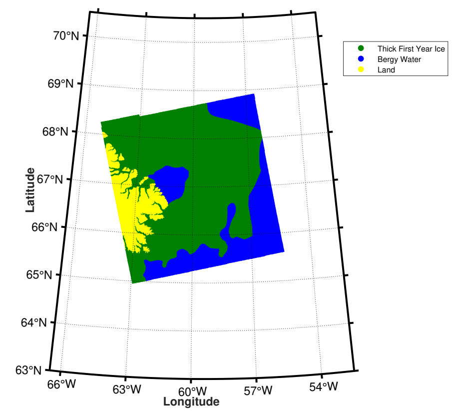

June 28 sea ice chart.

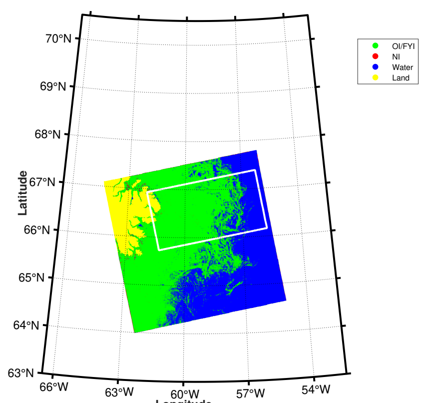

June 17 classification result.

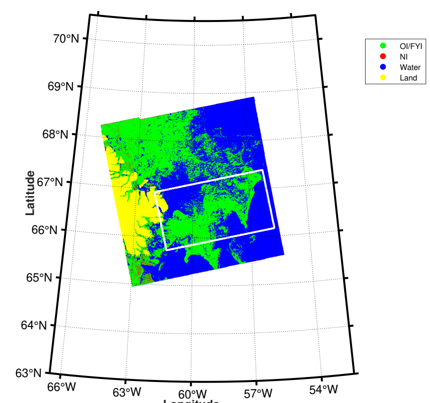

June 29 classification result.

Figure 2.17: June 17 and June 29, 2021.

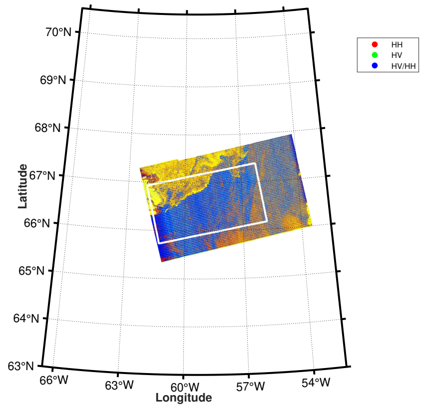

July 22 pseudo color image.

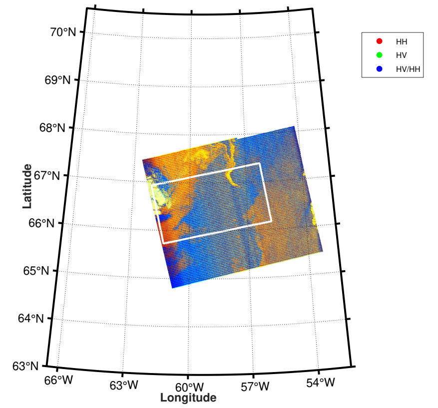

August 3 pseudo color image.

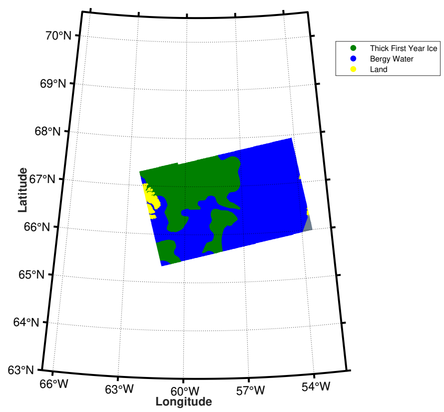

July 19 sea ice chart.

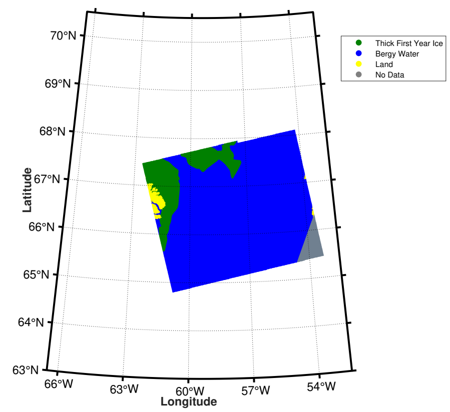

August 2 sea ice chart.

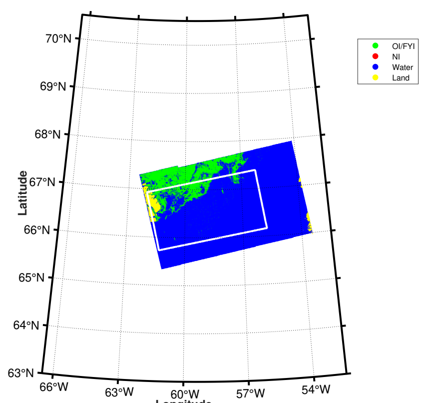

July 22 classification result.

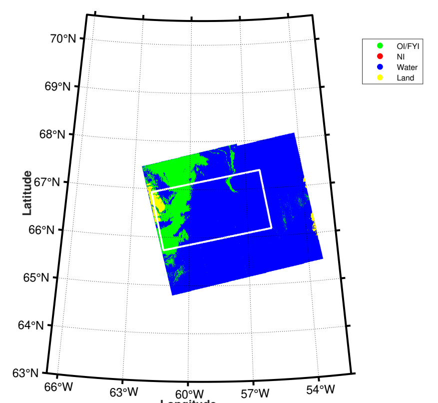

August 3 classification result.

Figure 2.18: July 22 and August 3, 2021.

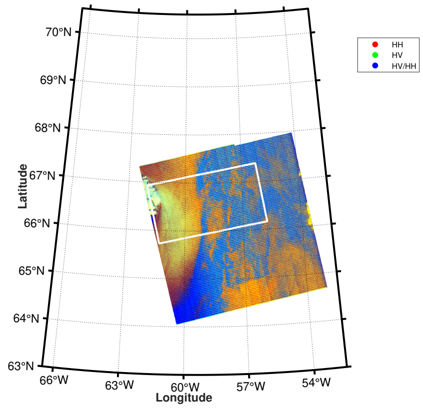

August 19 pseudo color image.

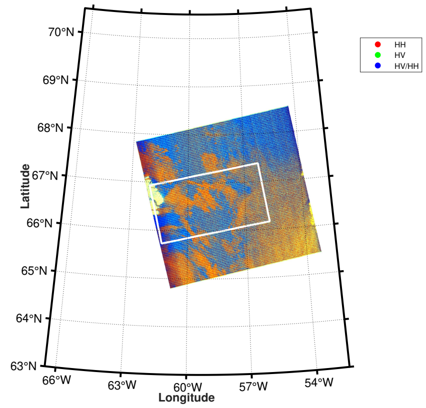

September 4 pseudo color image.

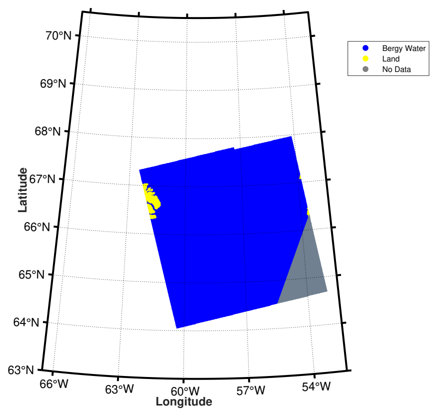

August 16 sea ice chart.

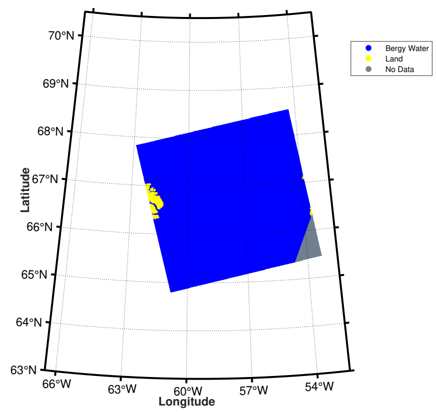

September 6 sea ice chart.

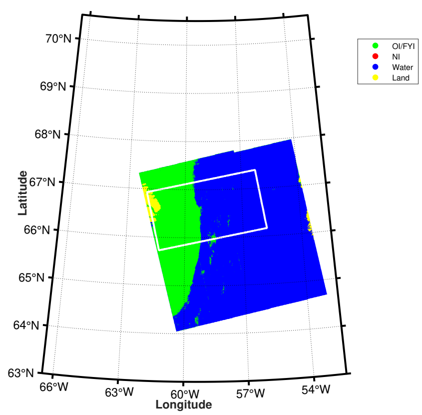

August 19 classification result.

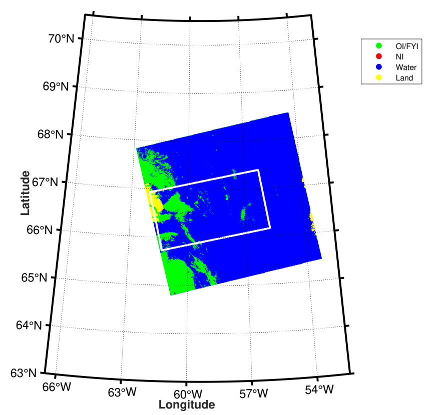

September 4 classification result.

Figure 2.19: August 19 and September 4, 2021.

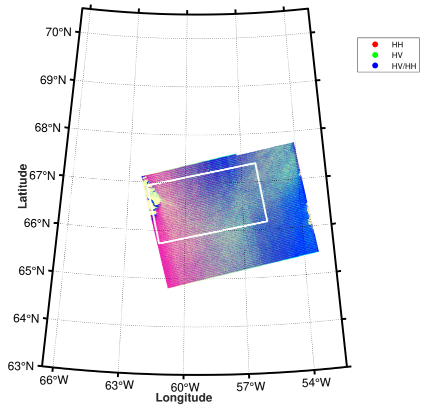

September 28 pseudo color image.

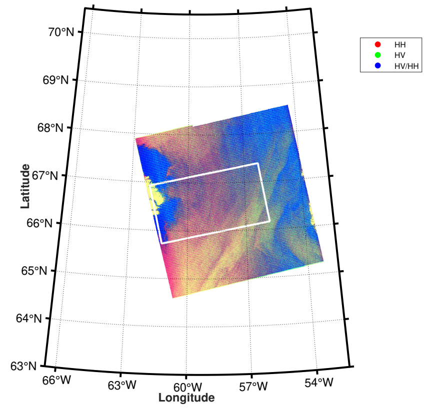

October 14 pseudo color image.

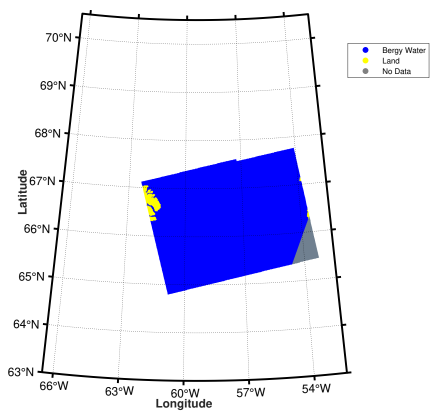

September 27 sea ice chart.

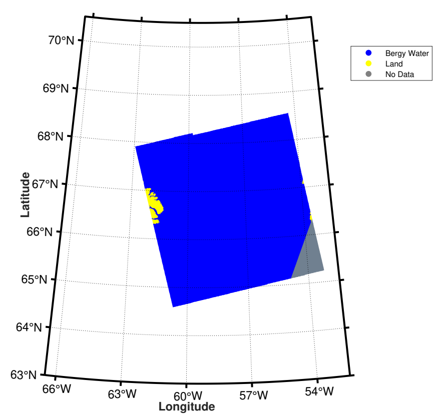

October 11 sea ice chart.

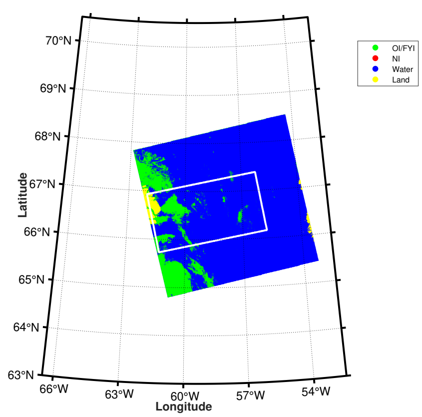

September 28 classification result.

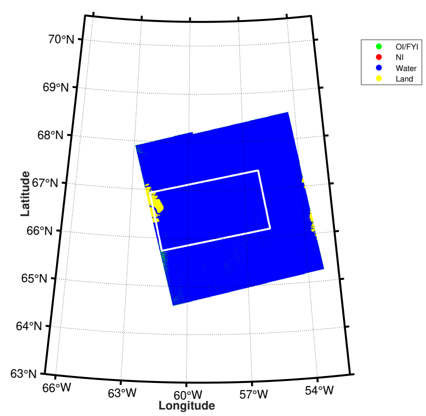

October 14 classification result.

Figure 2.20: September 28 and October 14, 2021.

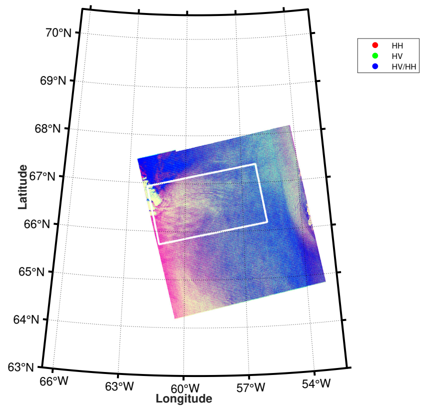

October 30 pseudo color image.

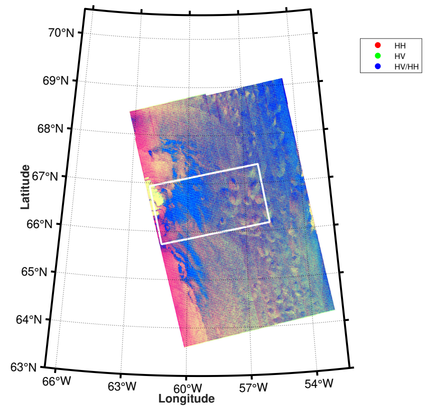

November 11 pseudo color image.

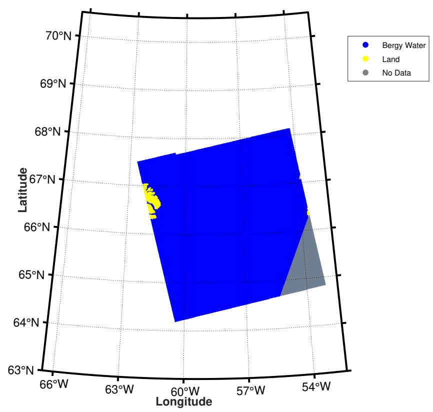

November 1 sea ice chart.

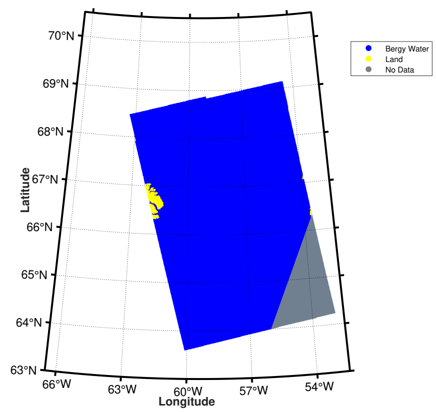

November 8 sea ice chart.

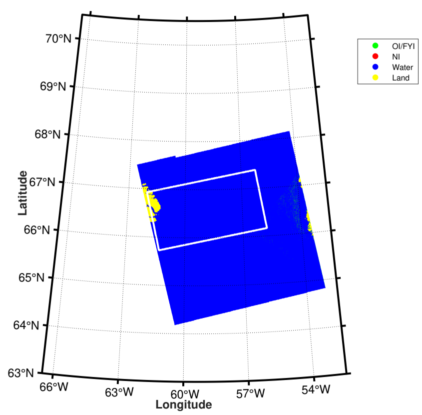

October 30 classification result.

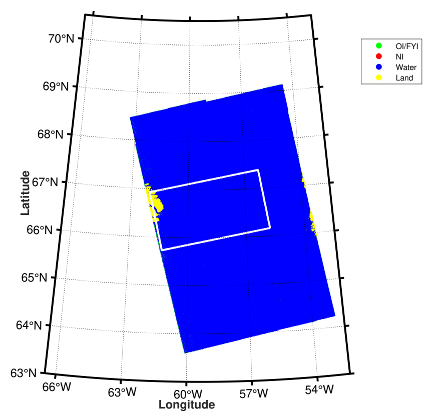

November 11 classification result.

Figure 2.21: October 30 and November 11, 2021.

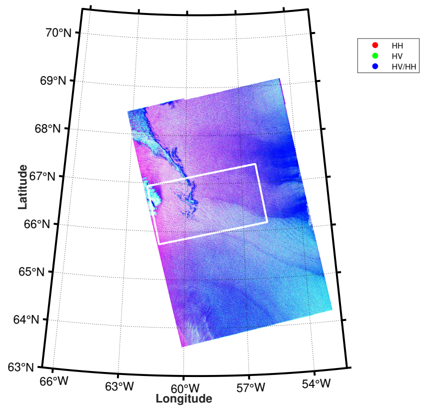

November 23 pseudo color image.

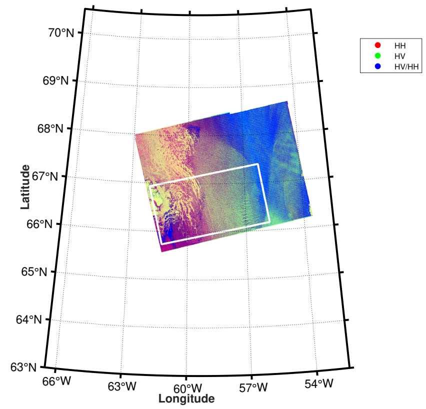

December 1 pseudo color image.

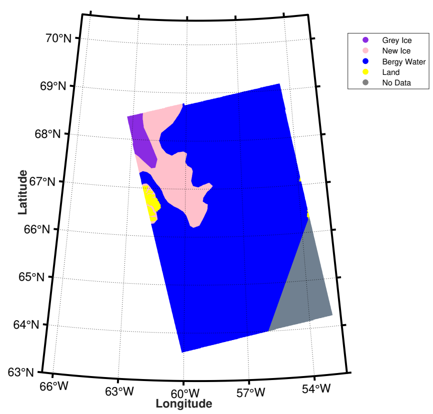

November 22 sea ice chart.

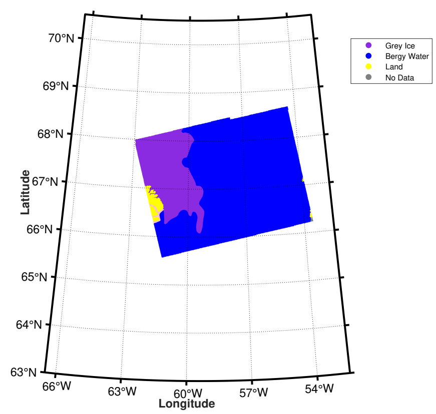

November 29 sea ice chart.

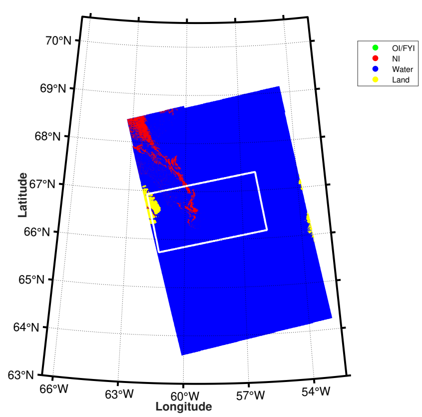

November 23 classification result.

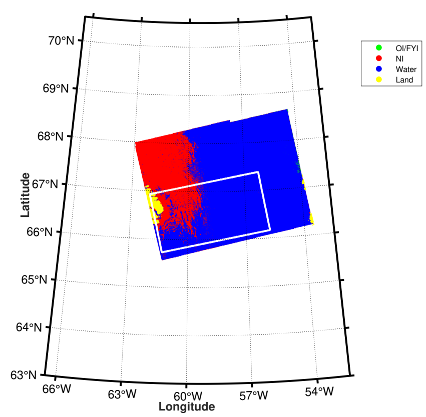

December 1 classification result.

Figure 2.22: November 23 and December 1, 2021.

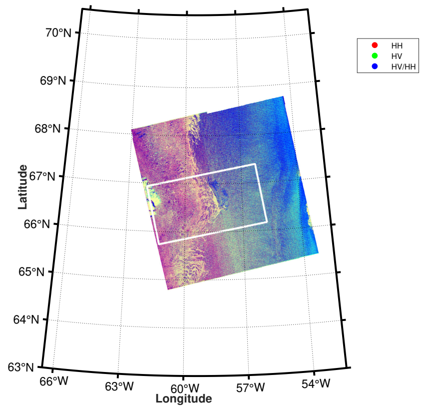

December 13 pseudo color image.

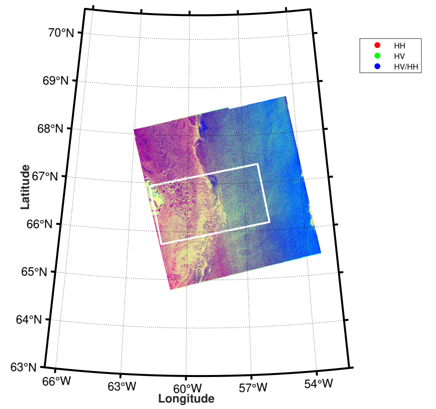

December 25 pseudo color image.

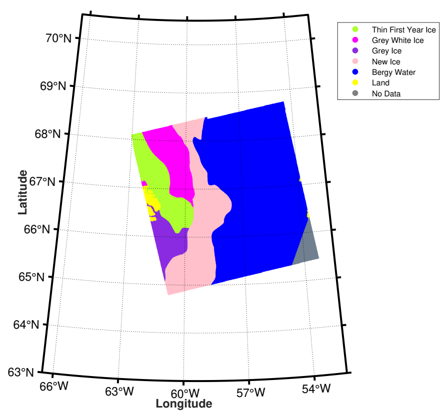

December 13 sea ice chart.

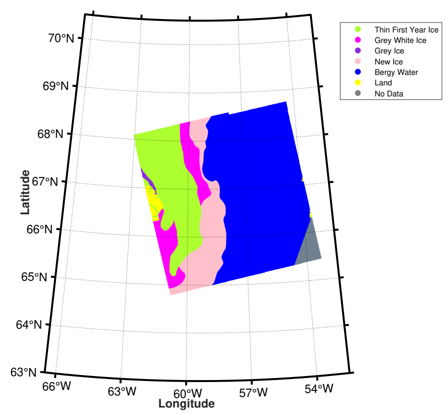

December 27 sea ice chart.

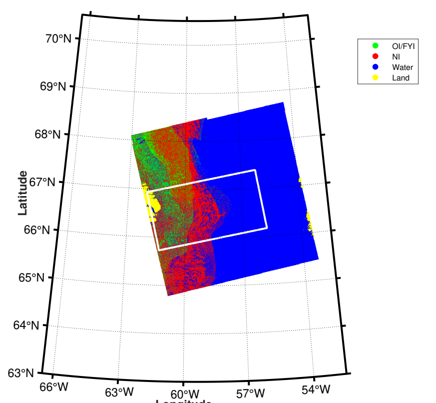

December 13 classification result.

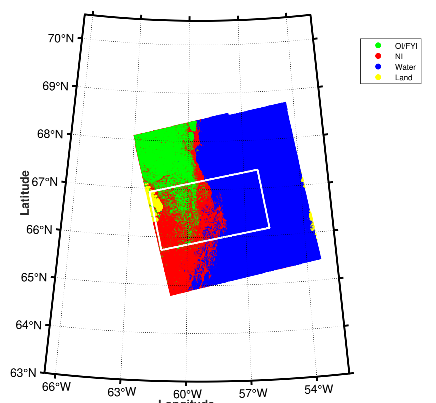

December 25 classification result.

Figure 2.23: December 13 and December 25, 2021.

sea ice classification over the conventional RF technique. Due to the learning algorithm difference between NFNet and RF, the former achieved higher overall sea ice classification accuracies (99.78% and 98.18% for two testing sets) compared to RF (87.42% and 78.73%), indicating the superiority of NFNet over the conventional RF technique based on the RCM data used here.

Chapter 3

Comparison of Sea Ice Classification From RADARSAT Constellation Mission and Sentinel-1 SAR Imagery

In this chapter, which is based on the conference paper [97][1], the sea ice classification results of RCM and Sentinel-1 SAR imagery from Davis Strait are compared. Samples from the overlapping area of dual-polarized (HH and HV) image pairs are used for the training and testing of the NFNet based classifier. This chapter is organized as follows. The RCM, Sentinel-1 and ground truth data are described in Section 3.1. The NFNet classifier and data preprocessing are introduced in Section 3.2. In Section 3.3, the classification results of RCM and Sentinel-1 are compared, followed by conclusions in Section 3.4.

[1] [97] H. Lyu, and W. Huang, "Comparison of sea ice classification from RCM and Sentinel-1 SAR imagery," in *Proc. IEEE 42nd Int. Geosci. Remote Sens. Symp.*, Kuala Lumpur, Malaysia, July 2022.

Author Contributions: All authors made substantial contributions to the conception and the design of the study. H.L. performed the experiments. W.H. and H.L. analyzed the data and wrote the paper. All authors reviewed and commented on the manuscript.

Table 3.1: RCM and Sentinel-1 images information.

Image Pair	Sensor	Acquisition Date	Polarizations	Beam Mode	Pixel Size
IP1	RCM	2021/1/4	HH	Medium Resolution 50m	20m
	Sentinel-1	2021/1/3	HV	EW GRD Medium Resolution 90m	40m
IP2	RCM	2021/1/25		Medium Resolution 50m	20m
	Sentinel-1	2021/1/24		EW GRD Medium Resolution 90m	40m
IP3	RCM	2021/3/1		Medium Resolution 50m	20m
	Sentinel-1	2021/2/8		EW GRD Medium Resolution 90m	40m
IP4	RCM	2020/12/28		Medium Resolution 50m	20m
	Sentinel-1	2020/12/28		EW GRD Medium Resolution 90m	40m
IP5	RCM	2021/1/18		Medium Resolution 50m	20m
	Sentinel-1	2021/1/18		EW GRD High Resolution 90m	40m
IP6	RCM	2021/2/15		Medium Resolution 50m	20m
	Sentinel-1	2021/2/15		EW GRD Medium Resolution 51m	25m

3.1 Data Description

3.1.1 Sea Ice Chart

The weekly regional ice charts were used as references to aid in the interpretation of the SAR images. Moreover, the classified ice types include OI/FYI, NI, and water, as mentioned in Chapter 2.1.

3.1.2 RCM and Sentinel-1 Data

Figure 3.1 illustrates the geographical location of the study area. RCM Medium Resolution 50m mode with a pixel size of 20 meters, Sentinel-1 EW GRD Medium Resolution mode with a pixel size of 40 meters and Sentinel-1 EW GRD High Resolution mode with a pixel size of 25 meters are adopted in this study. It should be noted that only one Sentinel image (IP6) with a pixel size of 25 meters was used in this study. Both RCM and Sentinel-1 C-band SARs operate at a center frequency of 5.405 GHz. The SAR images were acquired between late December 2020 and early March 2021 over the Davis Strait. Six pairs of images each of which contains a variety of sea ice cover types with fairly large overlapping areas and little time difference (no more than one day) are used here. The information of these pairs of RCM and Sentinel-1 images is summarized in Table 3.1. In Figure 3.1, the outlines of the

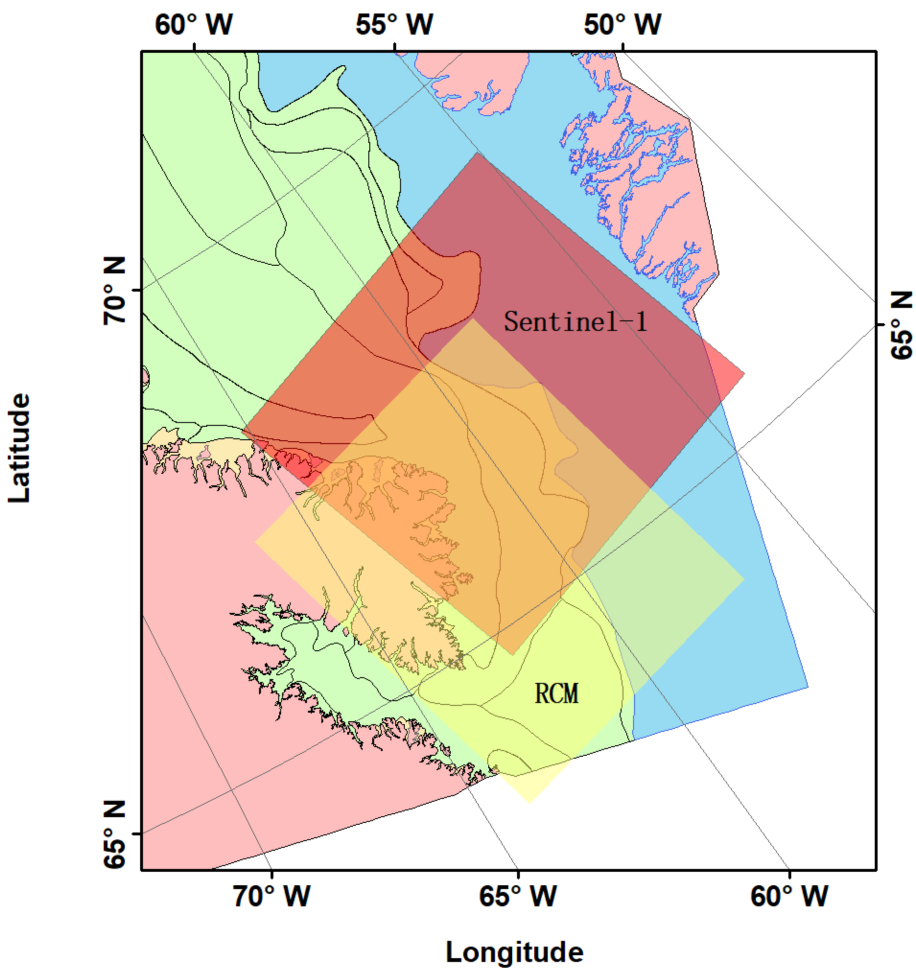

Figure 3.1: The locations of the fourth pair (IP4) of dual-polarized RCM and Sentinel-1 images laid over sea ice chart.

IP4 images from the RCM and Sentinel-1 are shown in red and yellow, respectively.

3.1.3 Training and Validation

In order to effectively compare the sea ice classification results of RCM and Sentinel-1 dual-polarization images, all the training and testing data are from their intersection area. IP1, IP2 and IP3 are used for selecting the training samples. All the testing samples are from IP4 since they are acquired from the same date and the overlapping area contains three cover types (OI/FYI, NI, and water). Images of IP5 and IP6 are used for additional comparison of RCM and Sentinel-1. Ten thousand samples are randomly selected for each cover type for the training and testing sets. The overlapping area of IP4 will be classified and compared in terms of overall accuracy, confusion matrix and OI/FYI and NI's sea ice concentration statistics for each sea ice chart polygon.

3.2 Methodology

The sea ice classification procedure in this study consists of preprocessing, splitting training and testing sets, model training, model evaluation, overlapping area extraction, sea ice classification and results comparison. The corresponding flowchart is illustrated in Figure 3.2. The techniques are described in detail in the following subsections.

3.2.1 Preprocessing

In this study, the SNAP [83] is employed to implement most preprocessing steps except thermal noise removal. The preprocessing steps for RCM raw data are the same as that in Chapter 2. For the Sentinel-1 EW data, the preprocessing workflow basically follows that in [98], which consists of the following steps: applying orbit file, thermal noise removal, border noise removal, calibration, speckle filtering and terrain correction. In our implementation, the simple destriping method and the SNAP thermal noise removal toolbox do not work well for mitigating the noise in the Sentinel-1 HV channel. Therefore, thermal noise removal from the standard preprocessing workflow for Sentinel-1 is replaced with the effective noise correction algorithm presented in [99]. The advanced thermal noise removal algorithm for Sentinel-1 EW mode was first presented in [86], which is to adjust the noise vectors by calculating the average noise scaling factor and inter-swath power balancing factor through segmented azimuthal blocks. However, the multiplicative noise still exists after denoising. Moreover, this method does not work well when using the average factors or applying the whole algorithm to a single image. The noise correction algorithm in [99] improves the method in [86] by splitting more azimuthal blocks, then factors are calculated based on local homogeneous regions. In this way, the noise correction process can be carried out effectively in a single image. In addition, the multiplicative noise is also removed in [99] based on the noise equivalent sigma zero (NESZ) file.

3.2.2 Normalizer-Free ResNet

The NFNet [75] is applied as the classifier to compare sea ice classification between RCM and Sentinel-1 dual-polarized data. In this research, its original 1000-way fully connected layer is replaced with a 3-way layer to match the sea ice types. The training strategy of the NFNet is basically the same as that in [75]. HH, HV and cross-polarization ratio are extracted as three channels from the RCM and Sentinel-1 overlapping areas as inputs. The patch size is set to 7×7. The sampled sub-regions are resized using bilinear interpolation to match the input size of the NFNet. The batch size, number of epoch and learning rate are set as 256, 150 and 0.01, separately. The final training models will be obtained according to the highest validation accuracy during the 150 epochs. For the training dataset, ten thousand samples for each cover type are manually selected from IP1-IP3 as explained in Section 2.3. 70% samples are used to train the model, and 30% samples are used for validation. The number of each cover type for the testing set is the same as that of the training set and they are only selected from the overlapping area of IP4.

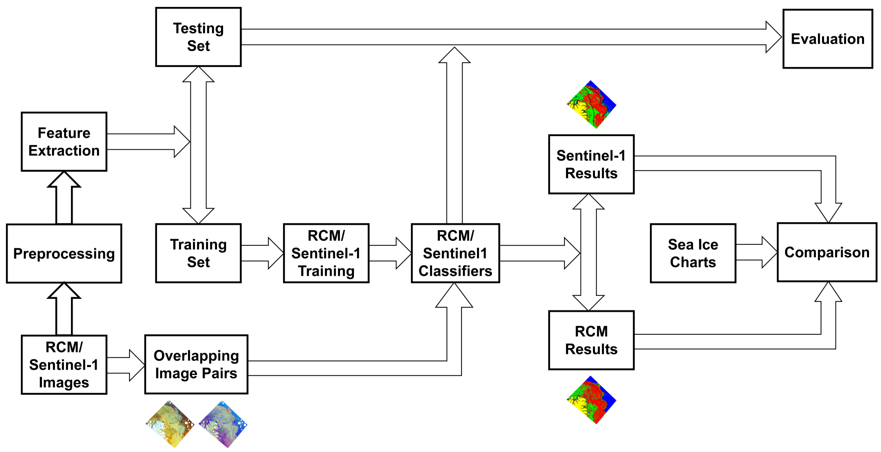

Figure 3.2: Flowchart of NFNet-based sea ice classification and results comparison.

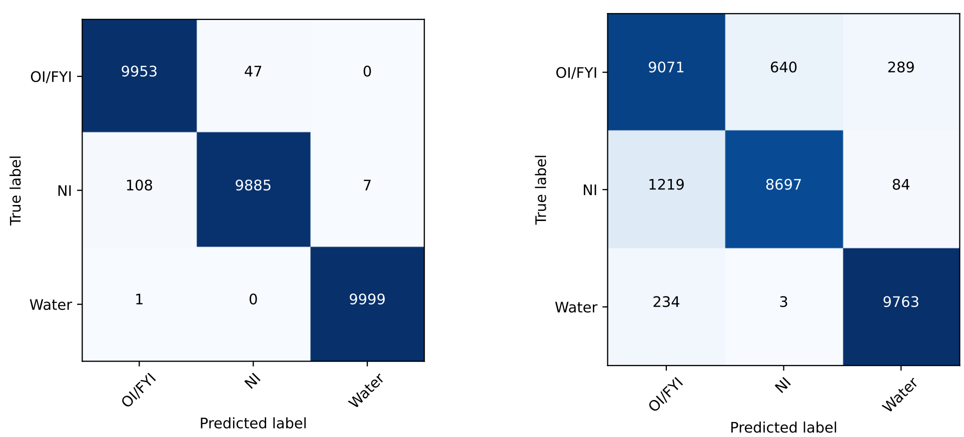

(a) RCM confusion matrix (IP4).

(b) Sentinel-1 confusion matrix (IP4).

Figure 3.3: Confusion matrices of the NFNet models trained from RCM and Sentinel-1 datasets.

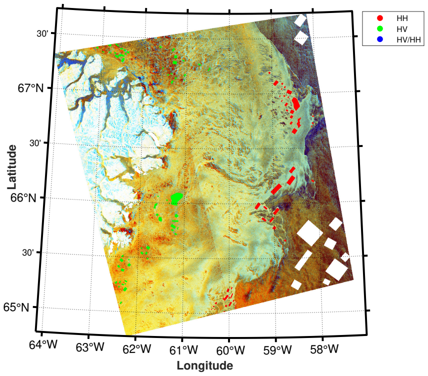

(a) Sentinel-1 Pseudo color image.

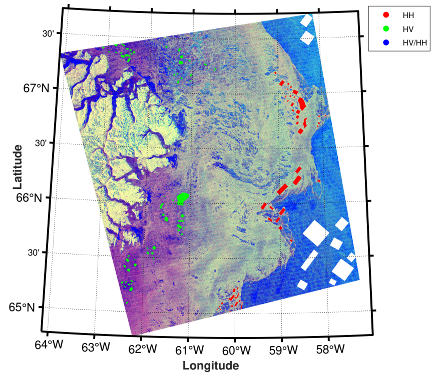

(b) RCM Pseudo color image.

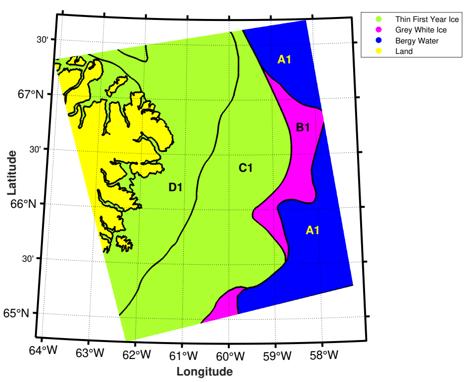

(c) Sea ice chart.

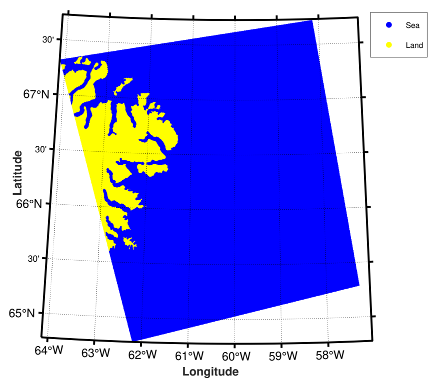

(d) Land mask.

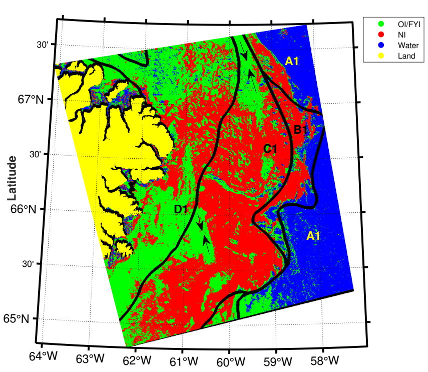

(e) Sentinel-1 classification result.

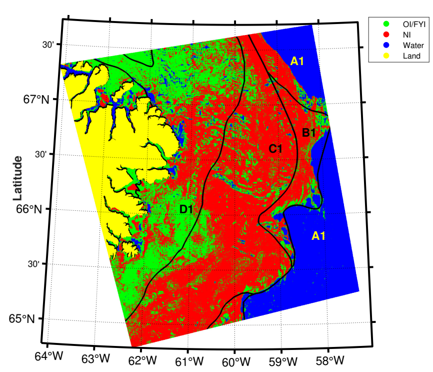

(f) RCM classification result.

Figure 3.4: (a) Sentinel-1 image acquired on December 28, 2020. (b) RCM image acquired on the same date. The green, red and white rectangles indicate the areas of the testing samples of OI/FYI, NI and water, respectively. (c) Sea ice chart. (d) Land mask. (e) Sentinel-1 classification result. (f) RCM classification result.

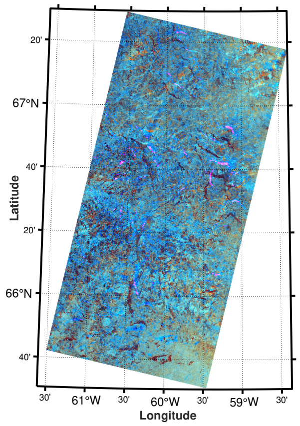

(a) Sentinel-1 pseudo color image.

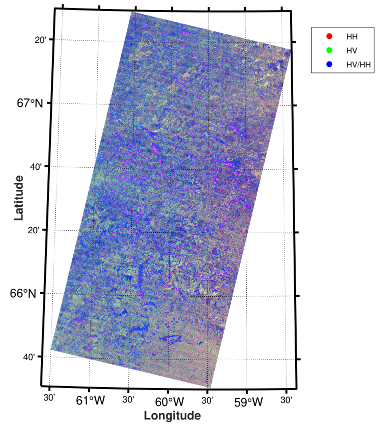

(b) RCM pseudo color image.

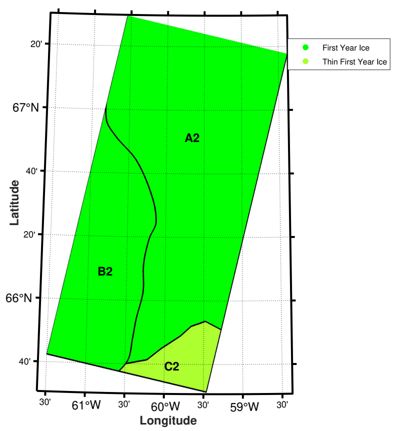

(c) Sea ice chart.

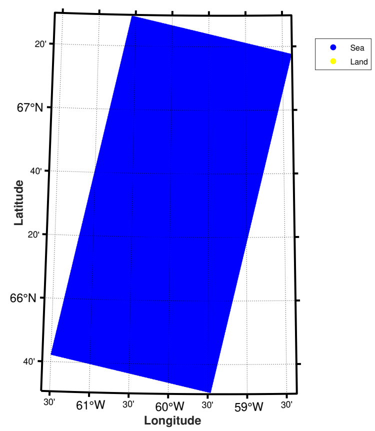

(d) Land mask.

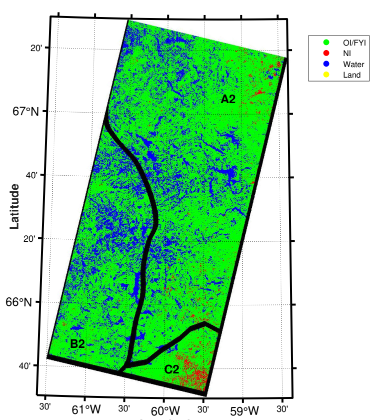

(e) Sentinel-1 classification result.

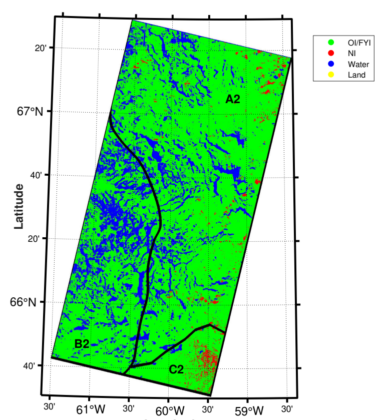

(f) RCM classification result.

Figure 3.5: (a) Sentinel-1 image acquired on January 18, 2021. (b) RCM image acquired on January 18, 2021. (c) Sea ice chart. (d) Land mask. (e) Sentinel-1 classification result. (f) RCM classification result.

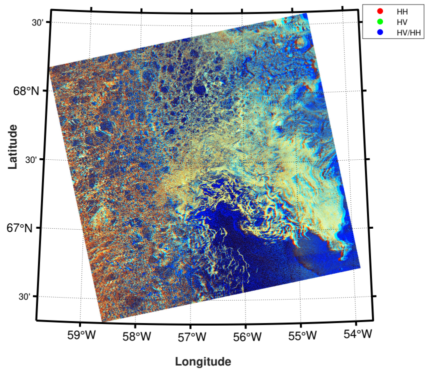

(a) Sentinel-1 pseudo color image.

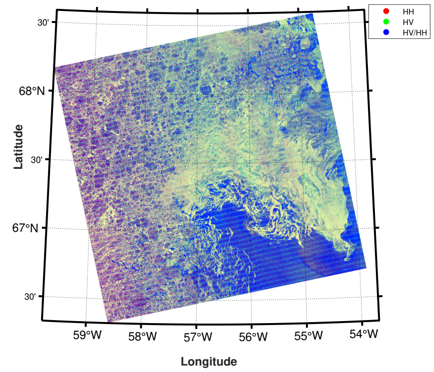

(b) RCM pseudo color image.

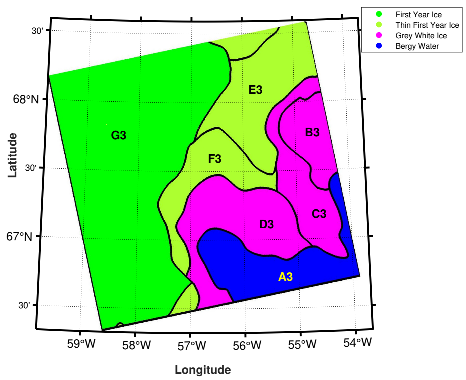

(c) Sea ice chart.

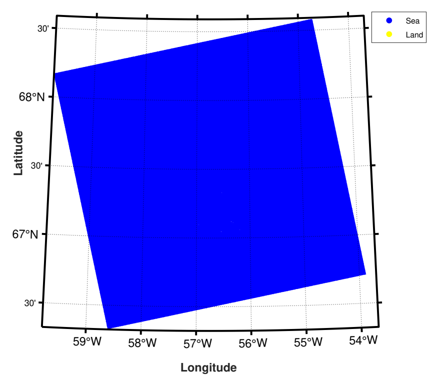

(d) Land mask.

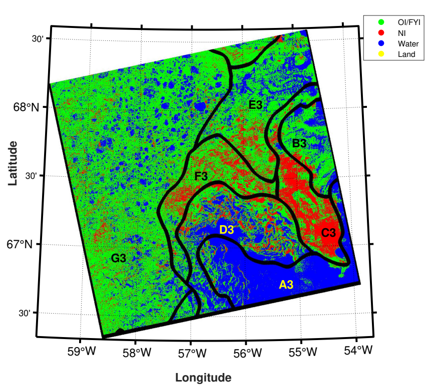

(e) Sentinel-1 classification result.

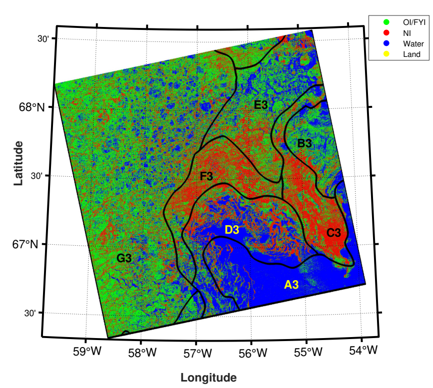

(f) RCM classification result.

Figure 3.6: (a) Sentinel-1 image acquired on February 15, 2021. (b) RCM image acquired on February 15, 2021. (c) Sea ice chart. (d) Land mask. (e) Sentinel-1 classification result. (f) RCM classification result.

3.3 Experiment Result

The overall accuracy and kappa coefficient of the NFNet classifier trained by RCM data are 99.46% and 0.9919, respectively. For the Sentinel-1 classifier, its overall accuracy is 91.77%, and the corresponding kappa coefficient is 0.8765. The overall accuracies and kappa coefficients show that the NFNet model trained with the RCM data can achieve higher accuracy than that of the Sentinel-1. In this study, the differences in resolution and thermal noise may be the reasons why the RCM-based model performs better than the Sentinel-1-based model. The thermal noise difference between RCM and Sentinel-1 will be investigated in future work. The corresponding confusion matrices are displayed in Figure 3.3. It can be seen that for the testing set of RCM, very few NI samples are misclassified as OI/FYI, while more than 1200 samples in the testing set of Sentinel-1 are misclassified as OI/FYI. The classifier trained by RCM performs well for OI/FYI and water classification. However, the Sentinel-1 model classifies more water samples as OI/FYI, and nearly 1000 samples of OI/FYI are identified as NI and water, respectively.

Figures 3.4, 3.5 and 3.6 illustrate the analysis results for IP4, IP5 and IP6, respectively. The green, red and white rectangles in Figures 3.4 (a) and (b) were used to select the testing samples of OI/FYI, NI and water, respectively. Ten thousand samples for each class of the testing set were obtained from the rectangles. The locations of testing samples in the RCM and Sentinel-1 images were the same. Tables 3.2, 3.3 and 3.4 present the comparison of the sea ice chart data, the Sentinel-1 and RCM results in terms of sea ice concentration.

Figure 3.4 demonstrates the classification results of the overlapping area for IP4. As mentioned earlier, the testing samples were selected from this image. Although noise correction techniques were applied, the noise caused by the banding effect (two wide strips from northwest to southeast in Figure 3.4 (a)) and the noise associated with the scalloping effect (narrow strips from southwest to northeast in Figure 3.4 (b)) are still evident. These noises may confuse the model during training, resulting in reduction of classification accuracy. In general, the classification results of the two images are similar, but more NI is identified

Table 3.2: Comparison of the estimated concentration results for IP4.

Region	**Area Ratio**	**Results**	**OI/FYI**	**NI**		**Total Concentration**
				GWI	**GI**	
A1	6.3%	Chart	0	0	0	<10%
		Sentinel-1	13.5%	6.6%		20.1%
		RCM	3.5%	11.3%		14.8%
B1	100%	Chart	20%	50%	20%	90%
		Sentinel-1	18.2%	46.2%		**64.4%**
		RCM	23.4%	58%		81.4%
C1	28.7%	Chart	70%	30%	0	90%+
		Sentinel-1	30.6%	**67.5%**		98.1%
		RCM	18.4%	**80.3%**		98.7%
D1	12.7%	Chart	90%+	0	0	90%+
		Sentinel-1	65.1%	**31.1%**		96.2%
		RCM	58.4%	**37.2%**		95.6%

Table 3.3: Comparison of the estimated concentration results for IP5.

Region	**Area Ratio**	**Results**	**FYI**		**NI**	**Total Concentration**
			MFYI	**TFYI**	**NI**	
A2	37%	Chart	50%	50%	0	90%+
		Sentinel-1	76.8%		1.8%	**78.6%**
		RCM	82%		1.7%	83.7%
B2	30.7%	Chart	50%	50%	0	90%+
		Sentinel-1	69.2%		0.5%	**69.7%**
		RCM	67.2%		0.2%	**67.4%**
C2	2.7%	Chart	0	90%+	0	90%+
		Sentinel-1	79.6%		**17.8%**	97.4%
		RCM	84.7%		**12.5%**	97.2%

Table 3.4: Comparison of the estimated concentration results for IP6.

Region	**Area Ratio**	**Results**	**FYI**		**NI**			**Total Concentration**
			MFYI	**TFYI**	**GWI**	**GI**	**NI**	
A3	7.8%	Chart	0	0	0	0	0	<10%
		Sentinel-1	11.9%		**2.4%**			14.3%
		RCM	9.1%		**5.1%**			14.2%
B3	34.8%	Chart	0	0	60%	20%	10%	90%
		Sentinel-1	60.3%		**9%**			**69.3%**
		RCM	48.1%		**17.7%**			**65.8%**
C3	97.5%	Chart	0	10%	40%	40%	0	90%
		Sentinel-1	37.4%		**53.1%**			90.5%
		RCM	32.5%		**55.2%**			87.7%
D3	24.2%	Chart		10%	40%	10%	0	60%
		Sentinel-1	38.5%		**16%**			54.5%
		RCM	25.4%		**26%**			51.4%
E3	64.3%	Chart	10%	80%	0	0	0	90%
		Sentinel-1	63.1%		12.2%			**75.3%**
		RCM	46.7%		25.5%			**72.2%**
F3	100%	Chart	0	90%+	0	0	0	90%+
		Sentinel-1	61.3%		**32.3%**			93.6%
		RCM	39.2%		**52.2%**			91.4%
G3	9%	Chart	90%+	0	0	0	0	90%+
		Sentinel-1	71.6%		8.7%			80.3%
		RCM	57.9%		**22.1%**			80%

in the RCM image. The black arrows in Figure 3.4 (e) indicate the two locations that are classified as OI/FYI in the Sentinel-1 image. Figure 3.4 (a) shows that the corresponding areas still have some thermal noise and these areas are bright white in the pseudo color image. Therefore, the classification result of Sentinel-1 is still affected by thermal noise, but the RCM NFNet model is more reliable for those areas. Table 3.2 shows the comparison of sea ice concentration results for the four polygons displayed in the sea ice chart (Figure 3.4 (c)). Region A1 is covered by water. Although the sea ice concentrations estimated from both RCM and Sentinel-1 are higher than 10%, it is evident that more water areas in the Sentinel-1 image are misclassified as ice. In regions C1 and D1, the NI percentages of the two results are significantly higher than that of the sea ice chart. Considering that the corresponding area ratios are very low, these two regions are not representative enough to be compared with the corresponding sea ice chart polygon. It is worth mentioning that the area ratio of region B1 is 100%. It can be observed that the edge of region B1 in the sea ice chart cannot match the edges of the ice area in both pseudo color images, indicating ice-free area exists in region B1. Thus, it is understandable that the classifier for RCM estimates that region B1's total concentration (81.4%) is less than 90%. However, the total concentration in region B1 estimated by the model for Sentinel-1 is much lower (64.4%) than that of the sea ice chart.

The classification results of IP5's overlapping area are displayed in Figures 3.5 (e) and (f). It can be seen this region is mainly covered by OI/FYI, and the identified NI and water areas from the two images are almost identical. Although no NI is reported in the sea ice chart, the areas (see top right and bottom right in Figures 3.5 (e) and (f)) classified as NI are similar in both results. In terms of total concentration, the estimated values in regions B2 and C2 based on the RCM and Sentinel-1 results are very close (see Table 3.3). More pixels in region A2 of the Sentinel-1 image are classified as water. However, the total concentration in region A2 of the RCM result is higher than that of the Sentinel-1 image and close to the corresponding concentration reported in the sea ice chart. From the perspective of NI concentration, the estimated results in regions A2 and B2 from the two results are very close. However, the Sentinel-1 model classified more NI in region C2. The NI concentration result of region A2 in the RCM image is lower but close to the concentration of the corresponding sea ice chart polygon.

Figures 3.6 (e) and (f) illustrate the classification results of the overlapping area of IP6. It should be noted that the Sentinel-1 image's resolution (51m) is higher than other Sentinel-1 images (90m) and similar to the resolution of RCM images (50m). In general, the total concentration results obtained from the two types of images are very close, while more areas of the RCM image are classified as NI. Based on the two classification results, the total concentrations of regions B3 and E3 are significantly lower than those in the sea ice chart. Considering the area ratios of these regions are low and the pseudo color images show some blue areas in these regions, the NFNet classification results should be more reliable. The NI concentrations of B3, C3, and D3 in the classified results are also lower than those of the sea ice chart polygons. Different sea ice conditions may cause a variation in backscattering characteristics for NI [48], and the training data may not represent all the types of NI in the regions, which could lead to the estimation difference in these regions. No NI is reported in E3, F3, and G3 from the sea ice chart. These regions are close to the NI regions (B3, C3, and D3) and both RCM and Sentinel-1 pseudo color images show bright areas in these regions. It is reasonable that the two classifiers trained by RCM and Sentinel-1 data could identify NI in these regions.

From the comparison of IP4 and IP5, it can be concluded that the results of RCM Medium resolution 50m images are closer to the sea ice chart than that of Sentinel-1 EW GRD Medium Resolution images. The higher resolution of RCM data may be one reason that leads to better performance. The result of the IP6 Sentinel-1 image demonstrates proper water and ice discrimination, which shows the potential generalization ability of NFNet for SAR images with different resolutions.

3.4 Chapter Summary

In this chapter, the sea ice classification results of RCM and Sentinel-1 dual-polarized data are compared. The NFNet classifiers for the two sensors use HH, HV, and cross polarization ratio as inputs and are trained by manually selected samples from the overlapping area. According to the data employed, good classification results of RCM prove that RCM Medium resolution 50m mode performs better than Sentinel-1 EW GRD Medium Resolution 90m mode for sea ice classification. The higher resolution of RCM may be one reason that leads to better performance. Although an advanced thermal noise removal algorithm is applied for the Sentinel-1 HV channel, its classification results may still be affected by thermal noise.

Bibliography

[1] *Manual of standard procedures for observing and reporting ice conditions*, Revised Ninth Edition, Canadian Ice Service, 2005.

[2] M. Heide-Jørgensen, H. Stern, and K. Laidre, "Dynamics of the sea ice edge in Davis Strait," *J. Mar. Syst.*, vol. 67, no. 1, pp. 170–178, Aug. 2007.

[3] M. Dirscherl, A. J. Dietz, S. Dech, and C. Kuenzer, "Remote sensing of ice motion in Antarctica – a review," *Remote Sens. Environ.*, vol. 237, pp. 111595, Feb. 2020.

[4] X. Yuan, "ENSO-related impacts on Antarctic sea ice: a synthesis of phenomenon and mechanisms," *Antarct. Sci.*, vol. 16, no. 4, pp. 415–425, Nov. 2004.

[5] P. R. Teleti and A. J. Luis, "Sea ice observations in polar regions: evolution of technologies in remote sensing," *Int. J. Geosci.*, vol. 4, no. 7, pp. 1031–1050, Sept. 2013.

[6] Y. S. Wu, C. Hannah, B. Petrie, R. Pettipas, I. Peterson, S. Prinsenberg, C. Lee, and R. Moritz, *Ocean current and sea ice statistics for Davis Strait.* St. John's, Canada: DFO, 2013.

[7] S. Anderson, "Remote sensing of the polar ice zones with HF radar," *Remote Sens.*, vol. 13, no. 21, pp. 4398, Oct. 2021.

[8] M. Shokr, *Sea ice : physics and remote sensing.* Washington, D.C., United States: AGU, 2015.

[9] L. Zhang, H. Liu, X. Gu, H. Guo, J. Chen, and G. Liu, "Sea ice classification using TerraSAR-X ScanSAR data with removal of scalloping and interscan banding," *IEEE J. Sel. Topics Appl. Earth Observ. Remote Sens.*, vol. 12, no. 2, pp. 589–598, Feb. 2019.

[10] W. Song, M. Li, Q. He, D. Huang, C. Perra, and A. Liotta, "A residual convolution neural network for sea ice classification with Sentinel-1 SAR imagery," in *Proc. IEEE Int. Conf. Data Min. Workshops*, Singapore, Nov. 2018, pp. 795-802.

[11] S. Nasonova, R. K. Scharien, T. Geldsetzer, S. E. L. Howell, and D. Power, "Optimal compact polarimetric parameters and texture features for discriminating sea ice types during winter and advanced melt," *Can. J. Remote Sens.*, vol. 44, no. 4, pp. 390–411, Sept. 2018.

[12] M. Dabboor, B. Montpetit, S. Howell, and C. Haas, "Improving sea ice characterization in dry ice winter conditions using polarimetric parameters from C- and L-band SAR data," *Remote Sens.*, vol. 9, no. 12, pp. 1270, Dec. 2017.

[13] A. S. Komarov and M. Buehner, "Automated detection of ice and open water from dual-polarization RADARSAT-2 images for data assimilation," *IEEE Trans. Geosci. Remote Sens.*, vol. 55, no. 10, pp. 5755–5769, Oct. 2017.

[14] H. Su, B. Ji, and Y. Wang, "Sea ice extent detection in the Bohai Sea using Sentinel-3 OLCI data," *Remote Sens.*, vol. 11, no. 20, pp. 2436, Oct. 2019.

[15] L. Shi, M. Li, C. Zhao, Z. Wang, Y. Shi, J. Zou, and T. Zeng, "Sea ice extent retrieval with HY-2A scatterometer data and its assessment," *Acta Oceanol. Sin.*, vol. 36, no. 8, pp. 76–83, July 2016.

[16] J. Karvonen, "Baltic sea ice concentration estimation based on C-band HH-polarized SAR data," *IEEE J. Sel. Topics Appl. Earth Observ. Remote Sens.*, vol. 5, no. 6, pp. 1874–1884, Dec. 2012.

[17] Y. Yang, E. DongChen, H. Wang, D. Chao, C. Hwang, F. Li, and S. Ai, "Sea ice concentration over the Antarctic ocean from satellite pulse altimetry," *Sci. China Earth Sci.*, vol. 54, no. 1, pp. 113–118, Jan. 2011.

[18] C. Kongoli, S.-A. Boukabara, B. Yan, F. Weng, and R. Ferraro, "A new sea-ice concentration algorithm based on microwave surface emissivities-application to AMSU measurements," *IEEE Trans. Geosci. Remote Sens.*, vol. 49, no. 1, pp. 175–189, Jan. 2011.

[19] N. MAAß and L. KALESCHKE, "Improving passive microwave sea ice concentration algorithms for coastal areas: applications to the Baltic Sea: improving sea ice algorithms in coastal regions," *Tellus A: Dyn. Meteorol. Oceanogr.*, vol. 62, no. 4, pp. 393–410, July 2010.

[20] H. Wakabayashi and S. Sakai, "Estimation of sea ice concentration in the Sea of Okhotsk using PALSAR polarimetric data," in *Proc. Int. Geosci. Remote Sens. Symp.*, Honolulu, HI, USA, July 2010, pp. 2398-2401.

[21] H. Su and Y. Wang, "Using MODIS data to estimate sea ice thickness in the Bohai Sea (China) in the 2009–2010 winter," *J. Geophys. Res. Oceans*, vol. 117, no. C10, pp. C10018, Oct. 2012.

[22] L. Kaleschke, X. Tian-Kunze, N. Maaß, M. Mäkynen, and M. Drusch, "Sea ice thickness retrieval from SMOS brightness temperatures during the Arctic freeze-up period," *Geophys. Res. Lett.*, vol. 39, no. 5, pp. L05501, Mar. 2012.

[23] T. Toyota, S. Ono, K. Cho, and K. I. Ohshima, "Retrieval of sea-ice thickness distribution in the Sea of Okhotsk from ALOS/PALSAR backscatter data," *Ann. Glaciol.*, vol. 52, no. 57, pp. 177–184, Sept. 2011.

[24] L. Kaleschke, N. Maaß, C. Haas, S. Hendricks, G. Heygster, and R. T. Tonboe, "A sea-ice thickness retrieval model for 1.4 GHz radiometry and application to airborne measurements over low salinity sea-ice," *Cryosphere*, vol. 4, no. 4, pp. 583–592, Dec. 2010.

[25] J.-W. Kim, D.-j. Kim, and B. J. Hwang, "Estimation of sea ice thickness in the Arctic Sea using polarimetric parameters of C- and X-band space-borne SAR data," in *Proc. IEEE Int. Geosci. Remote Sens. Symp.*, Honolulu, HI, USA, July 2010, pp. 2402-2405.

[26] T. Hollands, S. Linow, and W. Dierking, "Reliability measures for sea ice motion retrieval from synthetic aperture radar images," *IEEE J. Sel. Topics Appl. Earth Observ. Remote Sens.*, vol. 8, no. 1, pp. 67–75, Jan. 2015.

[27] A. Berg and L. E. B. Eriksson, "Investigation of a hybrid algorithm for sea ice drift measurements using synthetic aperture radar images," *IEEE Trans. Geosci. Remote Sens.*, vol. 52, no. 8, pp. 5023–5033, Aug. 2014.

[28] F. Girard-Ardhuin and R. Ezraty, "Enhanced Arctic sea ice drift estimation merging radiometer and scatterometer data," *IEEE Trans. Geosci. Remote Sens.*, vol. 50, no. 7, pp. 2639–2648, Feb. 2012.

[29] T. Hollands and W. Dierking, "Performance of a multiscale correlation algorithm for the estimation of sea-ice drift from SAR images: initial results," *Ann. Glaciol.*, vol. 52, no. 57, pp. 311–317, May 2011.

[30] T. Lavergne, S. Eastwood, Z. Teffah, H. Schyberg, and L.-A. Breivik, "Sea ice motion from low-resolution satellite sensors: an alternative method and its validation in the Arctic," *J. Geophys. Res. Oceans*, vol. 115, no. C10, pp. C10032, Oct. 2010.

[31] W. Dierking, "Sea ice monitoring by synthetic aperture radar," *Oceanogr.*, vol. 26, no. 5, pp. 100–111, June 2013.

[32] W. Song, M. Li, W. Gao, D. Huang, Z. Ma, A. Liotta, and C. Perra, "Automatic sea-ice classification of SAR images based on spatial and temporal features learning," *IEEE Trans. Geosci. Remote Sens.*, vol. 59, no. 12, pp. 9887–9901, Jan. 2021.

[33] Q. Yan and W. Huang, "Sea ice remote sensing using GNSS-R: a review," *Remote Sens.*, vol. 11, no. 21, pp. 2565, Nov. 2019.

[34] L. Sobisevich, V. Agafonov, D. Presnov, V. Gravirov, D. Likhodeev, and R. Zhostkov, "The advanced prototype of the Geohydroacoustic Ice Buoy," *Sensors*, vol. 20, no. 24, pp. 7213, Dec. 2020.

[35] A. Beitsch, S. Kern, and L. Kaleschke, "Comparison of SSM/I and AMSR-E sea ice concentrations with ASPeCt ship observations around Antarctica," *IEEE Trans. Geosci. Remote Sens.*, no. 4, pp. 1985–1996, Apr. 2015.

[36] S. Yuan, W. Shi, X. Liu, N. Xu, and W. Chen, "Erratum to: Ice type extraction of rough ice in the eastern coast of Liaodong Bay with shore-based radar," *Nat. Hazards Obs.*, vol. 77, no. 2, pp. 1415–1415, June 2015.

[37] L. Tian, H. Xie, S. F. Ackley, J. Tang, A. M. Mestas-Nunez, and X. Wang, "Sea-ice freeboard and thickness in the Ross Sea from airborne (IceBridge 2013) and satellite (ICESat 2003-2008) observations," *Ann. Glaciol.*, vol. 61, no. 82, pp. 24–39, Jan. 2020.

[38] Q. Yan and W. Huang, "Spaceborne GNSS-R sea ice detection using delay-doppler maps: first results from the U.K. TechDemoSat-1 mission," *IEEE J. Sel. Top. Appl. Earth Obs. Remote Sens.*, vol. 9, no. 10, pp. 4795–4801, Oct. 2016.

[39] S. de Roda Husman, "Polarimetric SAR signals of river ice breakup," M.S. thesis, Dept. Civil Eng. and Geosci., TU Delft Univ., Delft, Netherlands, 2020.

[40] A. A. Thompson, "Overview of the RADARSAT Constellation Mission," *Can. J. Remote Sens.*, vol. 41, no. 5, pp. 401–407, Sept. 2015.

[41] R. Kruk, M. C. Fuller, A. S. Komarov, D. Isleifson, and I. Jeffrey, "Proof of concept for sea ice stage of development classification using deep learning," *Remote Sens.*, vol. 12, no. 15, pp. 2486, Aug. 2020.

[42] A. M. Johansson, C. Brekke, G. Spreen, and J. A. King, "X-, C-, and L-band SAR signatures of newly formed sea ice in Arctic leads during winter and spring," *Remote Sens. Environ.*, vol. 204, pp. 162 – 180, Oct. 2017.

[43] N. Zakhvatkina, V. Smirnov, and I. Bychkova, "Satellite SAR data-based sea ice classification: an overview," *Geosci.*, vol. 9, no. 4, pp. 152, Feb. 2019.

[44] S. Sandven and O. M. Johannessen, *Sea Ice Monitoring by Remote Sensing.* Bethesda, MD, USA: ASPRS, 2006.

[45] R. Jobanputra and D. Clausi, "Texture analysis using Gaussian weighted grey level co-occurrence probabilities," in *Proc. 1st Can. Conf. Comput. and Robot Vision*, London, ON, Canada, May 2004, pp. 51-57.

[46] Q. Yu and D. A. Clausi, "SAR sea-ice image analysis based on iterative region growing using semantics," *IEEE Trans. Geosci. Remote Sens.*, vol. 45, no. 12, pp. 3919–3931, Dec. 2007.

[47] J. P. Gill, J. J. Yackel, and T. Geldsetzer, "Analysis of consistency in first-year sea ice classification potential of C-band SAR polarimetric parameters," *Can. J. Remote. Sens.*, vol. 39, no. 2, pp. 101–117, Mar. 2013.

[48] S. Singha, M. Johansson, N. Hughes, S. M. Hvidegaard, and H. Skourup, "Arctic sea ice characterization using spaceborne fully polarimetric L-, C-, and X-band SAR with validation by airborne measurements," *IEEE Trans. Geosci. Remote Sens.*, vol. 56, no. 7, pp. 3715–3734, July 2018.

[49] L. E. Eriksson et al., "Evaluation of new spaceborne SAR sensors for sea-ice monitoring in the Baltic Sea," *Can. J. Remote. Sens.*, vol. 36, no. sup1, pp. S56–S73, Jan. 2010.

[50] A. M. Johansson, J. A. King, A. P. Doulgeris, S. Gerland, S. Singha, G. Spreen, and T. Busche, "Combined observations of Arctic sea ice with near-coincident colocated X-band, C-band, and L-band SAR satellite remote sensing and helicopter-borne measurements," *J. Geophys. Res. Oceans*, vol. 122, no. 1, pp. 669–691, Jan. 2017.

[51] J. P. Gill and J. J. Yackel, "Evaluation of C-band SAR polarimetric parameters for discrimination of first-year sea ice types," *Can. J. Remote Sens.*, vol. 38, no. 3, pp. 306–323, Apr. 2012.

[52] R. K. Raney, R. Schulze, H. B. Sequeira, H. Winters, P. D. Spudis, B. Bussey, J. Crusan, J. R. Jensen, W. Marinelli, P. McKerracher, C. Neish, and M. Palsetia, "The lunar Mini-RF radars: Hybrid polarimetric architecture and initial results," *Proc. IEEE*, vol. 99, no. 5, pp. 808–823, May 2011.

[53] R. K. Raney, J. T. S. Cahill, G. W. Patterson, and D. B. J. Bussey, "The m-chi decomposition of hybrid dual-polarimetric radar data with application to lunar craters," *J. Geophys. Res. Planets*, vol. 117, no. E12, pp. E00H21, May 2012.

[54] B. Brisco, M. Mahdianpari, and F. Mohammadimanesh, "Hybrid compact polarimetric SAR for environmental monitoring with the RADARSAT constellation mission," *Remote Sens.*, vol. 12, no. 20, pp. 3283, Oct. 2020.

[55] M. Dabboor and T. Geldsetzer, "Towards sea ice classification using simulated RADARSAT Constellation Mission compact polarimetric SAR imagery," *Remote Sens. Environ.*, vol. 140, pp. 189–195, Jan. 2014.

[56] T. Geldsetzer, M. Arkett, T. Zagon, F. Charbonneau, J. J. Yackel, and R. K. Scharien, "All-season compact-polarimetry C-band SAR observations of sea ice," *Can. J. Remote. Sens.*, vol. 41, no. 5, pp. 485–504, Nov. 2015.

[57] H. Lyu, W. Huang, and M. Mahdianpari, "A meta-analysis of sea ice monitoring using spaceborne polarimetric SAR: advances in the last decade," *IEEE J. Sel. Top. Appl. Earth Obs. Remote Sens.*, vol. 15, pp. 6158–6179, July 2022.

[58] D. Huntley, D. Rotheram-Clarke, A. Pon, A. Tomaszewicz, J. Leighton, R. Cocking, and J. Joseph, "Benchmarked RADARSAT-2, SENTINEL-1 and RADARSAT Constellation Mission change-detection monitoring at North Slide, Thompson River Valley, British Columbia: ensuring a landslide-resilient national railway network," *Can. J. Remote Sens.*, vol. 47, no. 4, pp. 635–656, June 2021.

[59] B.-H. Choe, A. Blais-Stevens, S. Samsonov, and J. Dudley, “Sentinel-1 and RADARSAT Constellation Mission InSAR assessment of slope movements in the Southern Interior of British Columbia, Canada,” *Remote Sens.*, vol. 13, no. 19, pp. 3999, Oct. 2021.

[60] S. E. L. Howell, M. Brady, and A. S. Komarov, “Large-scale sea ice motion from Sentinel-1 and the RADARSAT Constellation Mission,” *Cryosphere Discuss.*, vol. 2021, no. EGU21-514, pp. 1–20, July 2021.

[61] A. S. Komarov and M. Buehner, “Sea ice concentration from the RADARSAT Constellation Mission for numerical sea ice prediction,” in *Proc. IEEE 19th Int. Symp. Antenna Technol. Appl. Electromagn*, Winnipeg, MB, Canada, Aug. 2021, pp. 1-2.

[62] W. Lang, J. Wu, X. Zhang, X. Yang, and J. Meng, “Detection of ice types in the Eastern Weddell Sea by fusing L- and C-band SIR-C polarimetric quantities,” *Int. J. Remote Sens.*, vol. 35, no. 19, pp. 6874–6893, July 2014.

[63] P. Ren, Z.-Q. Yu, G.-S. Dong, G.-X. Wang, and K. Wei, “Sea ice classification with first-order logic refined sliding bagging,” *J. Coast. Res.*, vol. 90, no. sp1, pp. 129–134, Sept. 2019.

[64] J.-W. Park, A. A. Korosov, M. Babiker, J.-S. Won, M. W. Hansen, and H.-C. Kim, “Classification of sea ice types in Sentinel-1 synthetic aperture radar images,” *Cryosphere*, vol. 14, no. 8, pp. 2629–2645, Aug. 2020.

[65] Z. Yu, T. Wang, X. Zhang, J. Zhang, and P. Ren, “Locality preserving fusion of multi-source images for sea-ice classification,” *Acta Oceanol. Sin.*, vol. 38, no. 7, pp. 129–136, July 2019.

[66] H. Han, J. Im, M. Kim, S. Sim, J. Kim, D.-j. Kim, and S.-H. Kang, “Retrieval of melt ponds on Arctic multiyear sea ice in summer from TerraSAR-X dual-polarization data using machine learning approaches: a case study in the Chukchi Sea with mid-incidence angle data,” *Remote Sens.*, vol. 8, no. 1, pp. 57, Jan. 2016.

[67] J. Lohse, A. P. Doulgeris, and W. Dierking, "An optimal decision-tree design strategy and its application to sea ice classification from SAR imagery," *Remote Sens.*, vol. 11, no. 13, pp. 1574, July 2019.

[68] C. L. V. Cooke and K. A. Scott, "Estimating sea ice concentration from SAR: training convolutional neural networks with passive microwave data," *IEEE Trans. Geosci. Remote Sens.*, vol. 57, no. 7, pp. 4735–4747, July 2019.

[69] M. Mahdianpari, B. Salehi, M. Rezaee, F. Mohammadimanesh, and Y. Zhang, "Very deep convolutional neural networks for complex land cover mapping using multispectral remote sensing imagery," *Remote Sens.*, vol. 10, no. 7, pp. 1119, July 2018.

[70] S. Fritzner, R. Graversen, and K. H. Christensen, "Assessment of high-resolution dynamical and machine learning models for prediction of sea ice concentration in a regional application," *J. Geophys. Res. Oceans*, vol. 125, no. 11, pp. 2020JC016277, Nov. 2020.

[71] Y. Han, C. Wei, R. Zhou, Z. Hong, Y. Zhang, and S. Yang, "Combining 3D-CNN and Squeeze-and-Excitation networks for remote sensing sea ice image classification," *Math. Probl. Eng.*, vol. 2020, pp. 1–15, Apr. 2020.

[72] S. Khaleghian, H. Ullah, T. Kræmer, N. Hughes, T. Eltoft, and A. Marinoni, "Sea ice classification of SAR imagery based on convolution neural networks," *Remote Sens.*, vol. 13, no. 9, pp. 1734, Apr. 2021.

[73] K. He, X. Zhang, S. Ren, and J. Sun, "Deep residual learning for image recognition," in *Proc. Conf. Comput. Vis. Pattern Recognit.*, Las Vegas, NV, USA, June 2016, pp. 770-778.

[74] "Image Classification on ImageNet." Papers with Code. https://paperswithcode.com (accessed Nov. 1st, 2021).

[75] A. Brock, S. De, S. L. Smith, and K. Simonyan, "High-performance large-scale image recognition without normalization," *CoRR*, Feb. 2021. [Online]. Available: https://arxiv.org/abs/2102.06171

[76] M.-A. N. Moen, A. P. Doulgeris, S. N. Anfinsen, A. H. H. Renner, N. Hughes, S. Gerland, and T. Eltoft, "Comparison of feature based segmentation of full polarimetric SAR satellite sea ice images with manually drawn ice charts," *Cryosphere*, vol. 7, no. 6, pp. 1693–1705, Nov. 2013.

[77] H. Lyu, W. Huang, and M. Mahdianpari, "Eastern Arctic sea ice sensing: First results from the RADARSAT Constellation Mission data," *Remote Sens.*, vol. 14, no. 5, pp. 1165, Feb. 2022.

[78] H. Lyu and W. Huang, "NFNet based sea ice classification from RADARSAT Constellation Mission data," in *Proc. 43rd Can. Symp. Remote Sens.*, Quebec, Canada, July 2022, pp. 1-4.

[79] H. Lyu, W. Huang, and M. Mahdianpari, "Sea ice detection from the RADARSAT Constellation Mission experiment data," in *Proc. IEEE 34th Can. Conf. Electr. Comput. Eng.*, ON, Canada, Sept. 2021, pp. 1-4.

[80] S. Singha, A. M. Johansson, and A. P. Doulgeris, "Robustness of SAR sea ice type classification across incidence angles and seasons at L-band," *IEEE Trans. Geosci. Remote Sens.*, vol. 59, no. 12, pp. 9941–9952, Nov. 2021.

[81] *ERA5 hourly data on single levels from 1979 to present*, Copernicus Climate Change Service Climate Data Store, June. 2018. [Online]. Available: https://cds.climate.copernicus.eu/cdsapp!/home

[82] "Weather information code table." Japan Oceanographic Data Center. https://www.jodc.go.jp/data_format/weather-code.html (accessed Oct. 25th, 2021).

[83] *Sentinel Application Platform*, (8.0.0), European Space Agency. Accessed: Oct. 19, 2020. [Online]. Available: http://step.esa.int/main

[84] *RADARSAT-2 product format definition*, D. MacDonald, Richmond, B.C., Canada, 2008.

[85] J.-S. Lee, J.-H. Wen, T. Ainsworth, K.-S. Chen, and A. Chen, “Improved sigma filter for speckle filtering of SAR imagery,” *IEEE Trans. Geosci. Remote Sens.*, vol. 47, no. 1, pp. 202–213, Jan. 2009.

[86] J.-W. Park, A. A. Korosov, M. Babiker, S. Sandven, and J.-S. Won, “Efficient thermal noise removal for Sentinel-1 TOPSAR cross-polarization channel,” *IEEE Trans. Geosci. Remote Sens.*, vol. 56, no. 3, pp. 1555–1565, Mar. 2018.

[87] J. G. Moik, *Digital processing of remotely sensed images.* Washington, D.C., USA: NASA, 1980.

[88] A. A. Bayanudin and R. H. Jatmiko, “Orthorectification of Sentinel-1 SAR (synthetic aperture radar) data in some parts of south-eastern Sulawesi using Sentinel-1 toolbox,” in *IOP Conf. Ser.: Earth Environ. Sci.*, Yogyakarta, Indonesia, Oct. 2016, vol. 47, no. 1, pp. 012007.

[89] R. Ressel, A. Frost, and S. Lehner, “A neural network-based classification for sea ice types on X-band SAR images,” *IEEE J. Sel. Top. Appl. Earth Obs. Remote Sens.*, vol. 8, no. 7, pp. 3672–3680, July 2015.

[90] S. Chen, M. Shokr, X. Li, Y. Ye, Z. Zhang, F. Hui, and X. Cheng, “MYI floes identification based on the texture and shape feature from dual-polarized Sentinel-1 imagery,” *Remote Sens.*, vol. 12, no. 19, pp. 3221, Oct. 2020.

[91] H. Tamiminia, B. Salehi, M. Mahdianpari, L. Quackenbush, S. Adeli, and B. Brisco, “Google Earth Engine for geo-big data applications: a meta-analysis and systematic review,” *ISPRS J. Photogramm. Remote Sens.*, vol. 164, pp. 152–170, June 2020.

[92] S. Leigh, Z. Wang, and D. A. Clausi, “Automated ice–water classification using dual polarization SAR satellite imagery,” *IEEE Trans. Geosci. Remote Sens.*, vol. 52, no. 9, pp. 5529–5539, Sept. 2014.

[93] Q. Yan and W. Huang, “Sea ice sensing from GNSS-R data using convolutional neural networks,” *IEEE Geosci. Remote Sens. Lett.*, vol. 15, no. 10, pp. 1510–1514, Oct. 2018.

[94] M. Sheykhmousa, M. Mahdianpari, H. Ghanbari, F. Mohammadimanesh, P. Ghamisi, and S. Homayouni, "Support vector machine versus random forest for remote sensing image classification: a meta-analysis and systematic review," *IEEE J. Sel. Top. Appl. Earth Obs. Remote Sens.*, vol. 13, pp. 6308–6325, Sept. 2020.

[95] L. Soh and C. Tsatsoulis, "Texture analysis of SAR sea ice imagery using gray level co-occurrence matrices," *IEEE Trans. Geosci. Remote Sens.*, vol. 37, no. 2, pp. 780–795, Mar. 1999.

[96] H. Liu, G. Huadong, and Z. Lu, "Sea ice classification using dual polarization SAR data," *IOP Conf. Ser.: Earth Environ. Sci.*, vol. 17, no. 1, pp. 012115, Mar. 2014.

[97] H. Lyu and W. Huang, "Comparison of sea ice classification from RCM and Sentinel-1 SAR imagery," in *Proc. IEEE 42nd Int. Geosci. Remote Sens. Symp.*, Kuala Lumpur, Malaysia, July 2022.

[98] F. Filipponi, "Sentinel-1 GRD preprocessing workflow," in *Proc. 3rd Int. Electron. Conf. Remote Sens.*, vol. 18, no. 1, June May 2019, pp. 11.

[99] Y. Sun and X.-M. Li, "Denoising Sentinel-1 extra-wide mode cross-polarization images over sea ice," *IEEE Trans. Geosci. Remote. Sens.*, vol. 59, no. 3, pp. 2116–2131, Mar. 2021.